Journal of Nanotechnology

Plasmonic Nanomaterials for Optical Sensor and Energy Storage and Transfer

Lead Guest Editor: Xuanhua Li
Guest Editors: Baofu Ding, Xingang Ren, and Yongxing Zhang

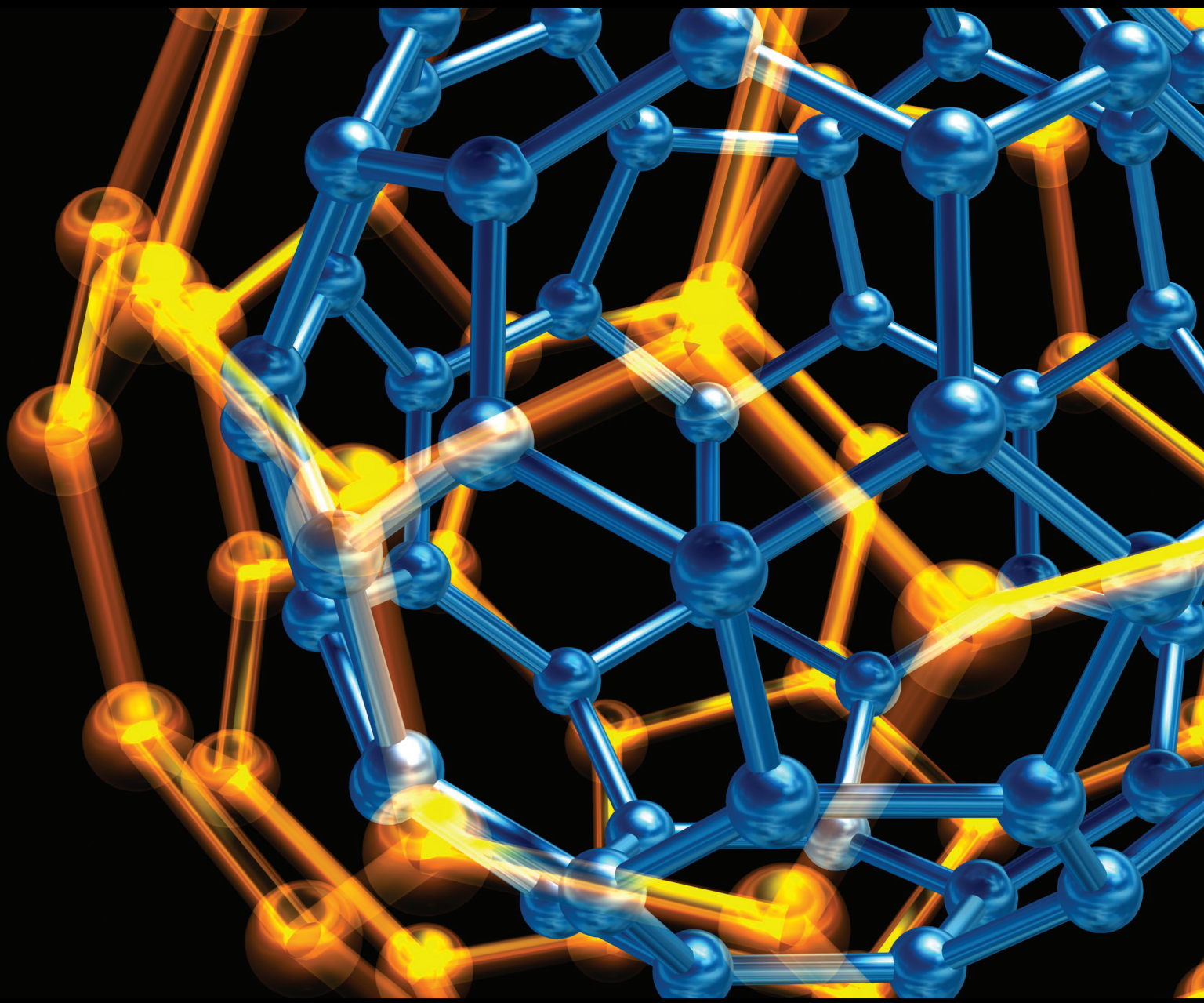

Plasmonic Nanomaterials for Optical Sensor and Energy Storage and Transfer

Journal of Nanotechnology

Plasmonic Nanomaterials for Optical Sensor and Energy Storage and Transfer

Lead Guest Editor: Xuanhua Li
Guest Editors: Baofu Ding, Xingang Ren, and Yongxing Zhang

Copyright © 2017 Hindawi. All rights reserved.

This is a special issue published in "Journal of Nanotechnology." All articles are open access articles distributed under the Creative Commons Attribution License, which permits unrestricted use, distribution, and reproduction in any medium, provided the original work is properly cited.

Editorial Board

S. J. Antony, UK
T. Baron, France
C. R. Cabrera, Puerto Rico
Enkeleda Dervishi, USA
Dmitriy A. Dikin, USA
Dimitris Drikakis, UK
Thomas Fischer, Germany
Noritada Kaji, Japan
Valery Khabashesku, USA
M. J. Lázaro, Spain
Eduard Llobet, Spain
Abdel Salam H. Makhlouf, USA
Paolo Milani, Italy
A. E. Miroshnichenko, Australia
Paresh Chandra Ray, USA
Marco Rossi, Italy
Jorge M. Seminario, USA
Xiaowei Sun, Singapore
Boris I. Yakobson, USA
Yoke K. Yap, USA
Chuan Jian Zhong, USA

Contents

Plasmonic Nanomaterials for Optical Sensor and Energy Storage and Transfer
Xuanhua Li, Baofu Ding, Xingang Ren, and Yongxing Zhang
Volume 2017, Article ID 6960707, 2 pages

Investigation of the Mode Structures of Multiphoton Induced Ultraviolet Laser in a ZnO Microrod
Guangping Zhu
Volume 2017, Article ID 3931210, 5 pages

Fabrication of Fiber Bragg Grating Coating with TiO_2 Nanostructured Metal Oxide for Refractive Index Sensor
Shaymaa Riyadh Tahhan, Rong Zhang Chen, Sheng Huang, Khalil I. Hajim, and Kevin P. Chen
Volume 2017, Article ID 2791282, 9 pages

Controllable Growth of the ZnO Nanorod Arrays on the Al Substrate and Their Reversible Wettability Transition
Hong Li, Hongyan Liu, Yushan Li, and Qinzhuang Liu
Volume 2017, Article ID 5104841, 4 pages

Effect of Vacancy Defects on the Electronic Structure and Optical Properties of GaN
Lili Cai and Cuiju Feng
Volume 2017, Article ID 6987430, 6 pages

Synthesis of $x\mathrm{LiMnPO_4}\cdot y\mathrm{Li_3V_2(PO_4)_3}$/C Nanocomposites for Lithium Ion Batteries Using Tributyl Phosphate as Phosphor Source
Yanming Wang, Bo Zhu, Xiaoyu Liu, and Fei Wang
Volume 2017, Article ID 4030249, 7 pages

Hindawi
Journal of Nanotechnology
Volume 2017, Article ID 6960707, 2 pages
https://doi.org/10.1155/2017/6960707

Editorial

Plasmonic Nanomaterials for Optical Sensor and Energy Storage and Transfer

Xuanhua Li,[1] Baofu Ding,[2] Xingang Ren,[3] and Yongxing Zhang[4]

[1]*School of Materials Science and Engineering, Northwestern Polytechnical University, Xi'an, China*
[2]*Department of Electrical and Electronic Engineering, Edith Cowan University, Joondalup, WA, Australia*
[3]*Department of Electrical and Electronic Engineering, University of Hong Kong, Pokfulam, Hong Kong*
[4]*School of Materials Science and Engineering, Huaibei Normal University, Huaibei, China*

Correspondence should be addressed to Xuanhua Li; lixh32@nwpu.edu.cn

Received 30 May 2017; Accepted 30 May 2017; Published 22 June 2017

Copyright © 2017 Xuanhua Li et al. This is an open access article distributed under the Creative Commons Attribution License, which permits unrestricted use, distribution, and reproduction in any medium, provided the original work is properly cited.

Nanomaterials including noble metal nanomaterials and some metal oxide nanomaterials exhibit very strong light-matter interactions under resonant excitation. Very large absorption and scattering at the localized wavelengths can been achieved. Because of their attractive optical properties, optical NPs and nanostructures have been commonly used in various fields from nanophotonics, analytical chemistry, biotechnology, and information storage to energy applications including photovoltaics and photocatalysis [1, 2].

Here, five original research articles seek to address the new preparation of optical nanomaterials, interesting design of optical sensor, and energy storage. Moreover, the new physical phenomena and mechanisms in these fields are discussed.

Dr. S. R. Tahhan and coworkers reported the fabrication of fiber Bragg grating coating with TiO_2 nanostructured metal oxide for refractive index sensor. Higher shifts and narrower peaks in the Bragg wavelength were obtained after coating the fiber with few hundreds nanometers thick TiO_2 coating of 20 nm–50 nm hole diameters. The sensitivity of the sensor with the TiO_2 coating is higher than that without coating due to the nanostructure's large surface area.

The mode structures of multiphoton induced ultraviolet laser in a ZnO microrod have been investigated by Dr. G. Zhu. Hexagonal wurtzite structural ZnO microrods were fabricated by vapor-phase transport method. Under the excitation of a pulse laser with 1200 nm wavelength, the multiphoton induced ultraviolet (UV) laser was observed in a microrod. The dependence of the laser mode structures on pump intensity was investigated. The result indicates that the laser belongs to whispering gallery mode (WGM) at low pump intensity and Fabry-Perot (FP) mode at high pump intensity.

Another work around controllable growth of the ZnO nanorod arrays has been reported by Dr. Q. Liu and coworkers. High quality ZnO nanorod arrays are formed using the ZnO nanoflakes on the Al substrates as seed layer. They found that a reversible wettability transition can be easily achieved via alternation of UV irradiation and dark storage. The physical adsorption of the water molecules on the surface of ZnO nanorod arrays is considered to be responsible for this transition, which is confirmed by X-ray photoelectron spectroscopy.

L. Cai and Dr. C. Feng have discussed the effect of vacancy defects on the electronic structure and optical properties of GaN using the generalized gradient approximation method within the density functional theory. The results show that the band gap increases in GaN with vacancy defects. Crystal parameters decrease in GaN with nitrogen vacancy (GaN:VN) and increase in GaN with gallium vacancy (GaN:VGa). The Ga vacancy introduces defect levels at the top of the valence band, and the defect levels are contributed by N2p electron states.

In addition, synthesis of *x*LiMnPO4·*y*Li3V2(PO4)3/C nanocomposites for lithium-ion batteries using tributyl phosphate as phosphor source has been reported by Dr. F. Wang and coworkers. They synthesized new *x*LiMnPO4·*y*Li3V2 (PO4)3/C nanocomposites, which is a very important issue for high-performance lithium-ion batteries.

The topic around optical properties of nanomaterials is very important and timely. They have been widely applied

in plasmon-enhanced spectroscopy, photocatalysis, energy storage, and solar cells. This topic is of relevance to the general research in chemistry, physics, optics, and material science and will attract great attentions of researchers in these fields who are new to or experienced in the plasmon-enhanced application in wide fields. Therefore, the potential broad audience of this issue will further promote the development of plasmon-related researches and accelerate their practical applications in various fields including surface-enhanced spectroscopy, energy storage, and energy transfer.

Xuanhua Li
Baofu Ding
Xingang Ren
Yongxing Zhang

References

[1] S. Guo, X. Li, J. Zhu, T. Tong, and B. Wei, "Au NPs@MoS_2 submicrometer sphere-ZnO nanorod hybrid structures for efficient photocatalytic hydrogen evolution with excellent stability," *Small*, vol. 12, no. 41, pp. 5692–5701, 2016.

[2] X. Li, S. Guo, C. Kan et al., "Au Multimer@MoS2 hybrid structures for efficient photocatalytical hydrogen production via strongly plasmonic coupling effect," *Nano Energy*, vol. 30, pp. 549–558, 2016.

Hindawi
Journal of Nanotechnology
Volume 2017, Article ID 3931210, 5 pages
https://doi.org/10.1155/2017/3931210

Research Article

Investigation of the Mode Structures of Multiphoton Induced Ultraviolet Laser in a ZnO Microrod

Guangping Zhu

School of Physics and Electronic Information, Huaibei Normal University, Huaibei 235000, China

Correspondence should be addressed to Guangping Zhu; gpzhu@chnu.edu.cn

Received 9 November 2016; Accepted 21 February 2017; Published 20 March 2017

Academic Editor: Baofu Ding

Copyright © 2017 Guangping Zhu. This is an open access article distributed under the Creative Commons Attribution License, which permits unrestricted use, distribution, and reproduction in any medium, provided the original work is properly cited.

Hexagonal wurtzite structural ZnO microrods were fabricated by vapor-phase transport method. Under the excitation of a pulse laser with 1200 nm wavelength, the multiphoton induced ultraviolet (UV) laser was observed in a microrod. The dependence of the laser mode structures on pump intensity was investigated. The result indicates that the laser belongs to whispering gallery mode (WGM) at low pump intensity and Fabry-Perot (FP) mode at high pump intensity. The corresponding positive feedback mechanisms were discussed.

1. Introduction

ZnO is a promising candidate for developing high efficiency ultraviolet optic-electronic devices operating at room temperature due to its wide band-gap and large exciton binding energy. Recent research progress in the fabrication of micro/nanostructured ZnO has created opportunities for developing micron-sized or nanosized optoelectronic devices. Optically pumped lasers have been achieved from various ZnO micro/nanostructures, such as thin films [1], powders [2], microtubes [3], nano/microwires [4–6], nanobelts [7], nanonails [8], microspheres [9], and nano/microdisks [10, 11] by single-photon absorption in which ZnO serves as both active gain medium and optical resonant cavity. On the other hand, multiphoton induced laser has also exhibited fascinating interest owing to high spatial resolution and large penetration depth of pump light. For 350 nm pump light, the single-photon absorption coefficient of ZnO attains 10^{-5} cm^{-1}, and the corresponding penetration depth is only 100 nm [12]. Therefore, the pump energy is mainly absorbed near the crystal surface, which limits largely the material availability. On the contrary, ZnO sample can be fully pumped in multiphoton excitation form by visible or infrared light due to high transmission.

At present, multiphoton induced laser in ZnO micro/nanostructures has aroused research interest due to a large nonlinear polarization coefficient. Two-photon and three-photon induced lasers have been reported in ZnO microneedle [13], nanodisk [14], and nanonail [15]. However, the report about the mode structure change with pump intensity has not been found. In this letter, three-photon induced ultraviolet laser is obtained in a ZnO microrod under excitation of 1200 nm infrared laser, and the dependence of mode structure on pump intensity will be discussed in detail.

2. Experiment

ZnO microrods were prepared by a simple vapor-phase transport method similar to our previous work [16]. The mixture of high pure zinc oxide and graphite powders was put at an end of a two-end-open quartz tube (2 cm diameter and 24 cm length) as source materials, and a silicon wafer was placed next to source materials as substrate. Afterwards, the quartz tube was put into a horizontal tube furnace. The reaction temperature of source material was set up at 1130°C and the reaction time was 30 min.

A femtosecond pulse laser with 1200 nm wavelength from an optical parametric oscillator (OPO) (repetition frequency 1000 Hz, pulse duration 150 fs) was focused into an ~100 μm diameter light spot onto the ZnO microrod sides. The output spectra were recorded by a fiber coupled optical multichannel analyzer (OMA) at room temperature.

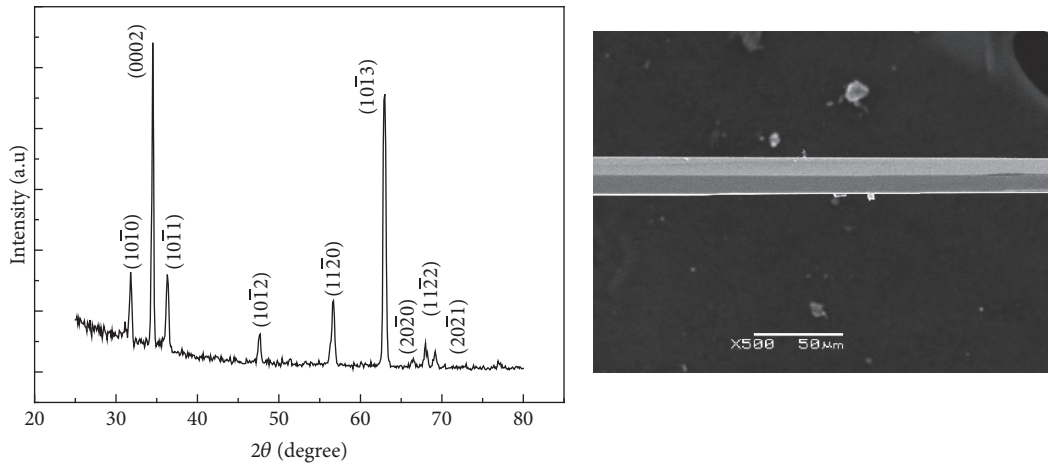

Figure 1: (a) The XRD pattern of the ZnO microrod and (b) the SEM image of the selected microrods for laser investigation.

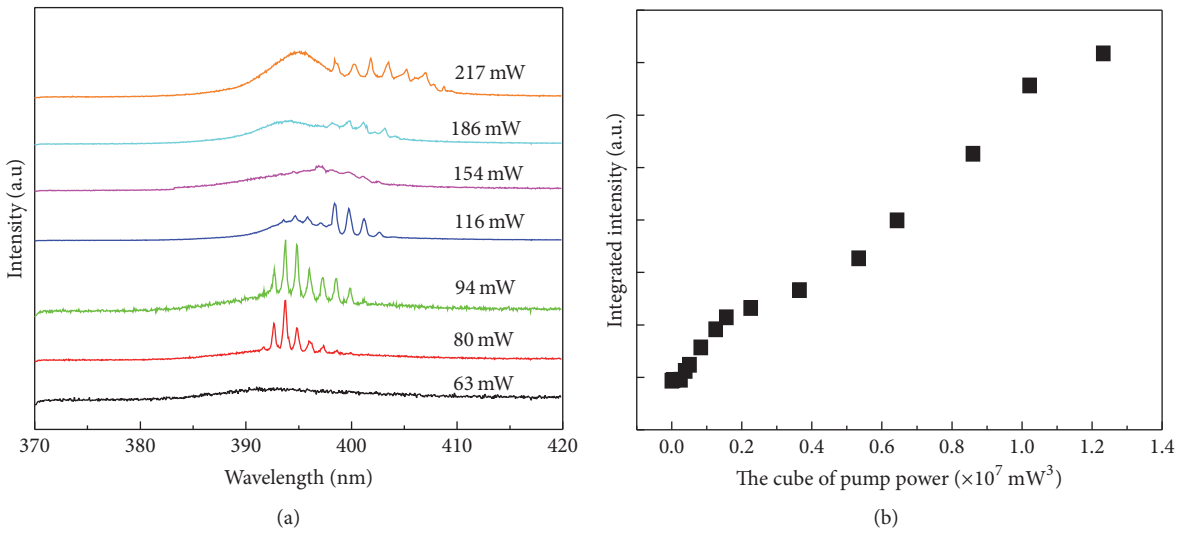

Figure 2: (a) The emission spectra at different pump power and (b) the variation of the spectrum integrated intensity with the cube of pump emission.

3. Result and Discussion

The XRD pattern of ZnO microrods is shown in Figure 1(a). All diffraction peaks in the figure match the crystal plane indexes of hexagonal wurtzite structural ZnO with lattice constants of $a = 0.325$ nm and $c = 0.521$ nm. The narrow diffraction peaks imply a high crystalline quality of the ZnO products. Figure 1(b) exhibits the SEM image of the selected microrod for laser investigation, which has a ~19 μm diagonal diameter.

Figure 2(a) shows the emission spectra at different pump power. At lower pump power of 63 mW, the spectrum exhibits a typical spontaneous emission band centered at 392 nm. When the pump power attains 80 mW, some narrow peaks appear in a range from 391 nm to 398 nm on the broad UV band, which indicates a lasing process occurring in the ZnO microrod. Under 94 mW pump power, the emission peaks are narrower and more peaks emerged in long wavelength edge. It is clearly that the UV lasers contain both exciton emission and electron-hole plasma (EHP) emission [17] at above lower excitation intensity. With pump power further increased to 116 mW, the exciton laser nearly disappeared, and only the EHP emissions exist in the laser modes. When the pump power attains 154 mW, no obvious laser modes can be observed. However, when the pump power rises to 186 mW, the laser modes appear once again, and with pump power increase, there are more modes in long wavelength edge. It is noted that the laser mode spacing obviously changes with the pump power increase. At lower excitation level, for example, 94 mW, although the mode spacing slightly varies with wavelength, the average mode spacing is only about 1.1 nm. However, at a higher pump power of 217 mW, the average mode spacing attains about 1.66 nm. In our experiment, the excitation wavelength is 1200 nm, and the

laser wavelength is about 400 nm. It can be believed that the lasing is generated by three-photon absorption. Figure 2(b) shows the curve of the emission intensity versus the cube of pump power. From the figure, two distinctly different lasing regions can be observed, one showing lower threshold and larger slope, whereas the other shows high threshold and small slope. The above discussion implies that the laser mechanism changes with pump intensity.

It has been known that the laser in ZnO crystal may be attributed to three types [2, 4, 5]: (a) random laser, (b) F-P laser, and (c) whispering gallery mode (WGM) laser. The random cavity model is put forward to explain the lasing in disordered ZnO mediums, which is attributed to recurrent scattering by localized photons. F-P resonant cavity model is introduced to interpret the laser modes in single wire/rod-like micro/nanostructure, in which two smooth end facets serve as cavity mirrors. For c-axis symmetrical hexagonal ZnO nanostructures, such as micro/nanodisks and microrods, the lasing mechanism can also result from whispering gallery cavity, in which the light wave can propagate circularly due to multiple total internal reflection caused by the six sides. In the three mechanisms, random cavity and F-P cavity cannot provide a high level of light confinement due to strong scattering and the large transmission, which result in a relatively low quality factor. On the other hand, WGM laser based on total internal reflection has unique properties, including low loss, narrow linewidth, and high quality factor.

It is obvious that the random laser cannot be generated in the ZnO microrod. Supposing that the laser originates from F-P cavity formed by two end facets of the microrod, and ignoring the variation of refractive index with wavelength, the laser mode spacing can be calculated according to the following equation:

$$\Delta\lambda = \frac{\lambda^2}{2nL}. \tag{1}$$

Here λ, n are wavelength and refractive index corresponding to some mode, and L is the length of the microrod. In our experiment, the microrod length is in magnitude order of millimeter and n is about 2.2 for 395 nm center wavelength; thus it can be estimated that the mode spacing is about 0.04 nm, which is far less than the experiment value, so the laser cannot also originate from F-P cavity formed by two end facets. Due to the high relative refractive index of ZnO to air for UV light, the six sides of the microrod can also construct the positive feedback cavity, which includes (1) F-P cavity in which the light bounces forth and back between the two opposite faces and (2) WGM cavity in which the light is fully reflected sequentially by the six sides of the microrod with a 60° incident angle. In order to further explain the positive feedback mechanism, the mode spacing of the laser for WG cavity and F-P cavity will be calculated in the following section, respectively.

For WGM laser, the resonant conditions of TE (the electric field is perpendicular to the symmetry axis of the microrod) and TM modes (the electric field is parallel to the symmetry axis of the microrod) can be deduced by Fresnel formula [13], which is expressed as follows:

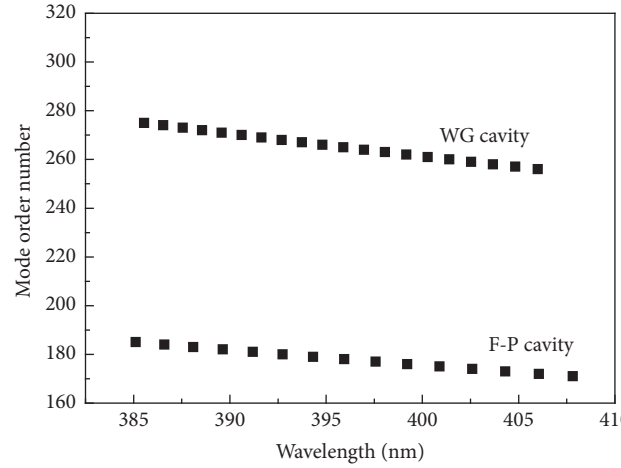

Figure 3: The calculation curve of mode order number versus wavelength in the case of F-P and WG cavity.

$$nL = \lambda\left(N + \frac{6}{\pi}\tan^{-1}\beta\sqrt{4n^2 - 3}\right). \tag{2}$$

In (2), N is mode order number, L the path length of a light circulation, and β factor depends on the laser polarization, $\beta = n$ for TE polarization and $\beta = 1/n$ for TM polarization. For F-P cavity laser, according to standing wave condition, the mode equation can be deduced as follows:

$$N\frac{\lambda}{2} = nL, \tag{3}$$

where L is the distance of the two opposite sides.

As a birefringent crystal, the refractive index of the wurtzite structural ZnO depends on the polarization. For TE and TM polarization, the refractive index can be expressed, respectively, as follows [18]:

$$\begin{aligned} n_{\mathrm{TE}} &= 1.916 + 1.145 \times 10^{-2}\,(h\nu)^2 + 1.6507 \\ &\quad \times 10^{-3}\,(h\nu)^4, \\ n_{\mathrm{TM}} &= 1.9384 + 1.1775 \times 10^{-2}\,(h\nu)^2 + 1.5237 \\ &\quad \times 10^{-3}\,(h\nu)^4. \end{aligned} \tag{4}$$

The unit of $h\nu$ is eV in (4).

The mode order numbers and corresponding wavelengths of TE and TM mode for WGM cavity and F-P cavity can be calculated by (2) and (4) or (3) and (4). According to Nobis et al. reports [18, 19], in needle-like or rod-like ZnO nanostructures, TM modes are main contents of WGM laser. So the modes observed should be TM modes in the experiment if the lasers originate from WG cavity. In our case, L is about 48 μm for WG cavity, the variation of the TM mode order number with wavelength can be calculated as shown in Figure 3. For F-P cavity, $L = 16$ μm, it can be deduced that the position of the Nth order TM mode is nearly the same as the $(N-1)$th TE mode. So, Figure 3 only shows TM mode order number variation with wavelength for F-P cavity. The average

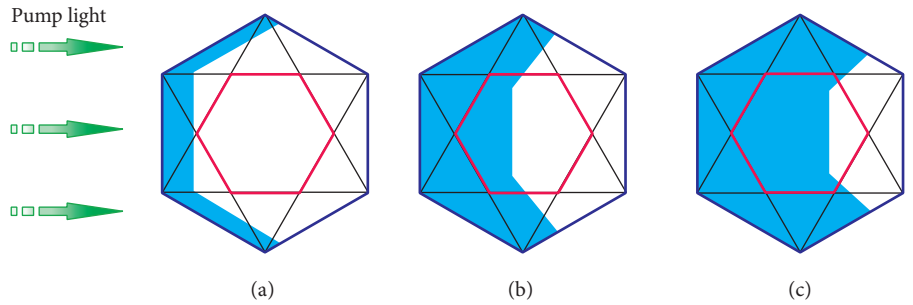

Figure 4: The change of multiphoton absorption region in the microrod with pump power increase: (a) low power; (b) higher power; (c) high power.

mode spacing is about 1.1 nm for WGM cavity and 1.7 nm for F-P cavity from Figure 3. Thus, it can be concluded that the lasing should originate from WG cavity at low pump intensity and F-P cavity at high pump intensity.

Based on the above discussion, an interpretation about laser mechanism variation with pump intensity is proposed. It is well known that the multiphoton absorption is highly sensitive to the intensity. In three-photon case, the absorption coefficient is proportional to cube of pump intensity. Figure 4 shows the region change of multiphoton absorption with pump intensity in the microrod, in which the region between the red and the blue hexagon is gain region of WG cavity. At lower pump level, only a thin layer medium near sides of the microrod can obtain enough excitation intensity to generate efficient multiphoton absorption due to the pump light attenuation with incident depth. The thin layer locates the gain region of WG cavity ($a \sim 4\,\mu$m depth near the sides of the microrod in our case). Because the loss of WG cavity is far less than that of F-P cavity, the laser will preferentially generate from WG cavity at lower excitation intensity, which explains the reason why the WGM lasers present at lower pump powers of 80 mW and 94 mW. Due to the depth increase of efficient multiphoton absorption at higher pump power (e.g., 116 mW), the multiphoton absorption can occur not only in the region near sides but also in center region. Thus, the luminescence from multiphoton absorption in the center region will deplete inversion population in the WGM gain region by amplified spontaneous emission (ASE), and lead WGM laser weakens. With further increase of pump power, the ASE can quench WGM laser, as is observed at 154 mW pump power. However, when the excitation intensity increases to a certain threshold once again, it is possible to generate F-P laser formed by two opposite sides because the EHP laser gain is proportional to the difference between EHP density and Mott density, although the F-P cavity loss is higher than WG cavity. It is the reason why the F-P laser can be observed at higher pump power of 186 mW and 217 mW. Of course, the laser mode spacing will be bigger than that of the WGM laser because the cavity length shortens relative to the WG cavity. It is noted that the exciton emission and EHP emission coexist in laser modes at lower pump intensity. The coexistence of excitonic lasing with the EHP lasing has been previously reported in ZnO thin film [20], which is attributed to the spatial distribution nonuniformity of the carriers in the sample. In our case, the coexistence of the two lasers can be attributed to the difference of the carrier density between the center and the edge of the pump light spot along length direction of the microrod (shown in Figure 5), because the pump light is close to Gauss light beam. At lower excitation level, it is possible that the carriers exist in EHP form in center region and in exciton form near edge of the pump spot due to their density difference, which will lead to the EHP laser and excitonic laser in different region. With excitation intensity increase, the EHP region outward spreads. So, the excitonic emission will weaken and the EHP emission enhance, which cause the spectrum red-shift in whole.

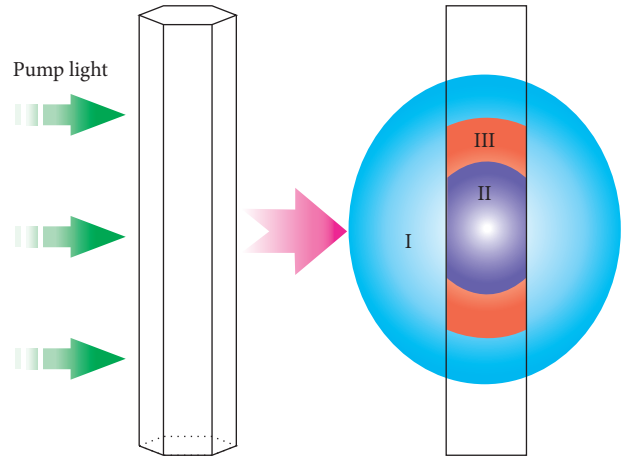

Figure 5: The change of carrier type along the microrod length direction: (I) pump light spot; (II) EHP region; (III) exciton region.

In single-photon excitation condition, ZnO lasing generally originates from the F-P cavity by two end facets of nano/microrod [1, 4], or WGM cavity by six sides [5, 18]. It is difficult to form F-P laser from the two opposite sides. This is due to the fact that the excitation light has a relatively small penetrating depth (about 100 nm for near-ultraviolet excitation light) and the excited carrier generally locates in WGM laser gain region of the nano/microrod with larger diameter (≥laser wavelength). Thus, the laser preferentially generates from WG cavity due to a smaller loss relative to F-P cavity. When the diameter of the rod is smaller than emission wavelength, scattering loss is very high and the WGM laser

usually cannot be generated. In this case, if the rod length is larger, the F-P cavity by two end facets can still generate enough gain. So, the lasing can be formed by the two end facets.

4. Conclusion

In conclusion, the ZnO microrods with hexagonal cross-section were fabricated by vapor-phase transport process, and an individual microrod was employed to construct a resonant cavity. Under the excitation of the 1200 nm nanosecond pulse laser, the three-photon excited UV laser was obtained. The result indicates that the lasing resonant mechanism varies with pump intensity. At lower excitation intensity, the exciton emission and EHP emission coexist in laser modes, and the lasers originated from a WGM cavity formed by the six sides of the ZnO microrod. At higher excitation intensity, the lasers were mainly generated from EHP emission, and the laser positive feedback was provided by F-P cavities by two opposite sides.

Conflicts of Interest

The author declares that there are no conflicts of interest regarding the publication of this paper.

Acknowledgments

This work was supported by the Key Foundation of Educational Commission of Anhui Province (KJ2016SD53).

References

[1] D. M. Bagnall, Y. F. Chen, Z. Zhu, T. Yao, M. Y. Shen, and T. Goto, "High temperature excitonic stimulated emission from ZnO epitaxial layers," *Applied Physics Letters*, vol. 73, no. 8, pp. 1038–1040, 1998.

[2] H. Cao, Y. G. Zhao, S. T. Ho, E. W. Seelig, Q. H. Wang, and R. P. Chang, "Random laser action in semiconductor powder," *Physical Review Letters*, vol. 82, no. 11, pp. 2278–2281, 1999.

[3] X. W. Sun, S. F. Yu, C. X. Xu, C. Yuen, B. J. Chen, and S. Li, "Room-temperature ultraviolet lasing from zinc oxide microtubes," *Japanese Journal of Applied Physics*, vol. 42, pp. L1229–L1231, 2003.

[4] M. H. Huang, S. Mao, H. Feick et al., "Room-temperature ultraviolet nanowire nanolasers," *Science*, vol. 292, no. 5523, pp. 1897–1899, 2001.

[5] C. Czekalla, C. Sturm, R. Schmidt-Grund, B. Cao, M. Lorenz, and M. Grundmann, "Whispering gallery mode lasing in zinc oxide microwires," *Applied Physics Letters*, vol. 92, no. 24, Article ID 241102, 2008.

[6] M. Ding, D. X. Zhao, B. Yao et al., "The ultraviolet laser from individual ZnO microwire with quadrate cross section," *Optics Express*, vol. 20, no. 13, pp. 13657–13662, 2012.

[7] B. S. Zou, R. B. Liu, F. F. Wang, A. L. Pan, L. Cao, and Z. L. Wang, "Lasing mechanism of ZnO nanowires/nanobelts at room temperature," *The Journal of Physical Chemistry B*, vol. 110, no. 26, pp. 12865–12873, 2006.

[8] D. Wang, H. W. Seo, C.-C. Tin et al., "Lasing in whispering gallery mode in ZnO nanonails," *Journal of Applied Physics*, vol. 99, no. 9, Article ID 093112, 2006.

[9] S. Okamoto, Y. Minowa, and M. Ashida, "White-light lasing in ZnO microspheres fabricated by laser ablation," in *Oxide-Based Materials and Devices III, 82630K*, vol. 8263 of *Proceedings of SPIE*, San Francisco, Calif, USA, January 2012.

[10] D. Yu, Y. Chen, B. Li et al., "Structural and lasing characteristics of ultrathin hexagonal ZnO nanodisks grown vertically on silicon-on-insulator substrates," *Applied Physics Letters*, vol. 91, no. 9, Article ID 091116, 2007.

[11] X. Liu, W. Fang, Y. Huang et al., "Optically pumped ultraviolet microdisk laser on a silicon substrate," *Applied Physics Letters*, vol. 84, no. 14, pp. 2488–2490, 2004.

[12] E. V. Chelnokov, N. M. Bityurin, and W. Marine, "Two-photon pumped zinc oxide random laser," in *Proceedings of the Topical Problems of Nonlinear Wave Physics*, vol. 5975 of *Proceedings of SPIE*, February 2006.

[13] G. P. Zhu, C. X. Xu, J. Zhu, C. G. Lv, and Y. P. Cui, "Two-photon excited whispering-gallery mode ultraviolet laser from an individual ZnO microneedle," *Applied Physics Letters*, vol. 94, no. 5, Article ID 051106, 2009.

[14] C. F. Zhang, F. Zhang, T. Xia et al., "Low-threshold two-photon pumped ZnO nanowire lasers," *Optics Express*, vol. 17, no. 10, pp. 7893–7900, 2009.

[15] J. Dai, C. X. Xu, and X. W. Sun, "Single-photon and three-photon absorption induced whispering-gallery mode lasing in ZnO micronails," *Optics Communications*, vol. 284, no. 16-17, pp. 4018–4021, 2011.

[16] G. P. Zhu, C. X. Xu, J. Zhu, and M. H. Wang, "Growth mechanism and multiphoton-induced photoluminescence of crownlike zinc oxide," *Journal of Materials Science*, vol. 46, no. 6, pp. 1877–1883, 2011.

[17] Z. K. Tang, M. Kawasaki, A. Ohtomo, H. Koinuma, and Y. Segawa, "Self-assembled ZnO nano-crystals and exciton lasing at room temperature," *Journal of Crystal Growth*, vol. 287, no. 1, pp. 169–179, 2006.

[18] T. Nobis and M. Grundmann, "Low-order optical whispering-gallery modes in hexagonal nanocavities," *Physical Review A*, vol. 72, no. 6, Article ID 063806, 2005.

[19] I. Braun, G. Ihlein, F. Laeri et al., "Hexagonal microlasers based on organic dyes in nanoporous crystals," *Applied Physics B: Lasers and Optics*, vol. 70, no. 3, pp. 335–343, 2000.

[20] Ü. Özgür, A. Teke, C. Liu, S. Cho, H. Morkoç, and H. O. Everitt, "Stimulated emission and time-resolved photoluminescence in rf-sputtered ZnO thin films," *Applied Physics Letters*, vol. 84, no. 17, pp. 3223–3225, 2004.

Hindawi
Journal of Nanotechnology
Volume 2017, Article ID 2791282, 9 pages
https://doi.org/10.1155/2017/2791282

Research Article

Fabrication of Fiber Bragg Grating Coating with TiO_2 Nanostructured Metal Oxide for Refractive Index Sensor

Shaymaa Riyadh Tahhan,[1] Rong Zhang Chen,[2] Sheng Huang,[2] Khalil I. Hajim,[3] and Kevin P. Chen[2]

[1]*Laser and Optoelectronics Engineering Department, College of Engineering, Nahrain University, Al-Jadriya, Baghdad, Iraq*
[2]*Department of Electrical and Computer Engineering, University of Pittsburgh, Pittsburgh, PA, USA*
[3]*Dijlah University, Baghdad, Iraq*

Correspondence should be addressed to Shaymaa Riyadh Tahhan; shaymaa.riyadh@gmail.com

Received 1 October 2016; Accepted 4 January 2017; Published 16 March 2017

Academic Editor: Baofu Ding

Copyright © 2017 Shaymaa Riyadh Tahhan et al. This is an open access article distributed under the Creative Commons Attribution License, which permits unrestricted use, distribution, and reproduction in any medium, provided the original work is properly cited.

To increase the sensitivity of biosensor a new approach using an optical fiber Bragg grating (FBG) coated with a suitable nanostructured metal oxide (NMO) is proposed which is costly effective compared to other biosensors. Bragg grating was written on a D-shaped optical fiber by phase mask method using a 248 nm KrF excimer laser for a 5 min exposure time producing a grating with a period of 528 nm. Titanium dioxide (TiO_2) nanostructured metal oxide was coated over the fiber for the purpose of increasing its sensing area. The etched D-shaped FBG was then coated with 312 nm thick TiO_2 nanostructured layer to ensure propagating the radiation modes within the core. The final structure was used to sense deionized water and saline. The etched D-shaped FBG original sensitivity before coating to air-deionized water and to air-saline was 0.314 nm/riu and 0.142 nm/riu, respectively. After coating the sensitivity became 1.257 nm/riu for air-deionized water and 0.857 nm/riu for air-saline.

1. Introduction

Swanton et al. in 1996 used the phase mask method to write uniform photorefractive FBG [1]. To enhance the written FBGs, high pressure hydrogen gas (H_2) was loaded in the optical fiber to increase the UV photosensitivity before writing the grating [2]. A novel approach of designing a chemosensor, based on cladding etched Bragg grating, was reported by Zhou et al. in 2004, where the FBG sensitivity to the refractive index of surrounding medium increases by HF etching. A measured sensitivity of 0.02 nm/% was obtained for different sugar solution concentrations [3]. FBG was coated with different thicknesses of SiO_2 nanoparticle mesoporous thin films and used as a refractive index sensor. This sensor showed a high sensitivity of 1927 nm/riu to RI changes with a response time shorter than 2 sec [4]. Specific and highly sensitive chemical sensors for in-water monitoring were made by coating fiber long period gratings with a nanoscale Syndiotactic Polystyrene (sPS) in nanoporous crystalline form by dip coating technique [5]. Other methods of coating were used to fabricate an optical chemical sensor in which the etched region of FBG was coated by a thin layer of gold nanoparticles to detect and determine the manganese concentration in water [6]. FBG was coated with different film thicknesses of gold by sputtering deposition technique and using it as a chemical sensor for ethanol in aqueous solution. It was found that the 50 nm gold film enhances the evanescent wave on the optical fiber surface and increases its sensitivity to detect ethanol with different concentrations [7].

Mantzila and Prodromidis in 2005 [8] anodically formed films of titanium oxide at 0.5–65 V in 1 M H_2SO_4 for 1 h under mild stirring. The films were characterized by electrochemical impedance spectroscopy, scanning electron microscopy, Raman spectroscopy, ellipsometry, and diffuse reflectance FT-IR spectroscopy.

Davies et al. in 2008 [11] were the first to investigate the sol-gel coated FBG for refractive index sensors. The sol-gel was made from titanium and silicon oxide coatings. The

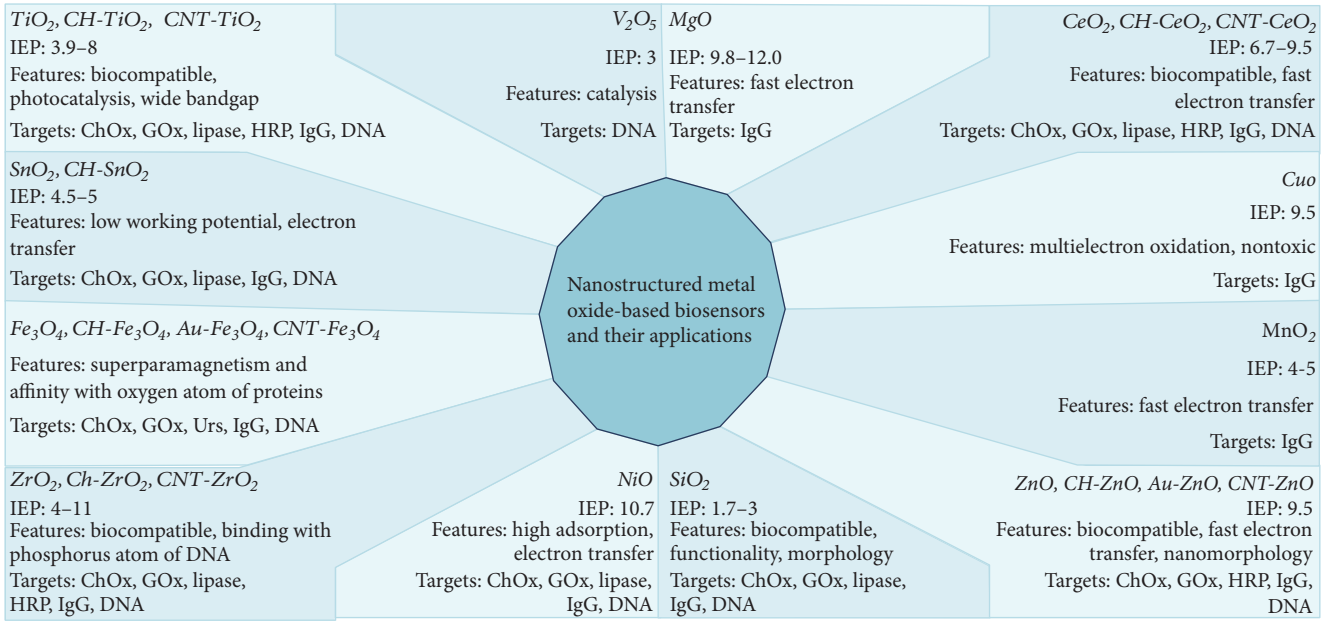

Figure 1: Nanostructured metal oxide-based biosensors and their applications (IEP, isoelectric point; ChOx, cholesterol oxidase; GOx, glucose oxidase; HRP, horseradish peroxidase; IgG, Immunoglobulin G; Urs, urease) [9].

results revealed a refractive index sensitivity dependence on thickness and index of the coating. The sensitivity of the coated FBG was higher than the uncoated region.

In 2010, Mun et al. [12] stated that optical interferometry of TiO_2 thin film array of nanotubes allows label free sensing of rabbit immunoglobulin G (IgG) by using protein A as a capture probe, immobilized on the nanotubes inner pore walls by electrostatic adsorption.

Liang et al. in 2011 [13] proved that the FBG sensitivity is based on the effective index for the waveguided mode. This sensitivity depends on the refractive index change of the ambient medium and the Bragg wavelength shift.

In the same year, Smietana et al. [14] presented the temperature sensing properties of a silicon nitride (SiNx) nanocoated long period grating. The SiNx nanocoating was applied to tune the external refractive index sensitivity of LPG, written with UV and electric arc technique. This work presented for the first time a nanocoating capable of simultaneously tuning the RI sensitivity and enabling temperature measurements in high-RI liquids applied to LPGs.

In 2012, Chen [15] studied and used the FBG sensors for extreme environments. They also used the KrF excimer laser to write the FBG by the phase mask method.

In 2013, Zhang et al. [16] coated the FBG with a bimaterial microscale using laser assisted maskless microdeposition and electroless nickel plating. Bimaterial coating enhanced the sensitivity of the FBG; the temperature sensitivity was doubled as compared to bare FBG.

In the same year, Ho et al. [17] designed a FBG sensor to detect the presence of the water entering concrete structures after being cracked by environmental effects. This work represents the first experiment tested the repeatability of the sensor to cyclic input of various volumes of water, and it tested the sensor's response to flooding conditions. The sensor had a good repeatability with fast response time <10 min.

The present work is concerned with the study of the performance of FBG coated with NMO materials to sense biomaterials. The main purpose of this research using the TiO_2-NMO with FBG is to enhance its sensitivity feature reaching to the sensing of so many diseases which cannot be detected conventionally.

The prepared FBG coated with TiO_2 NMO (20 nm holes diameter) may be used in antibody sensing if we use the protein type A (5 nm diameter) to fill the pores of the TiO_2 NMO and then bind with the antibody type IgG1 and IgG2 leading to highly likely related Bragg shift corresponding to expected variation in the effective index.

The main interest is to prepare cost effective, small size, and less cumbersome biosensor. Large sensing area of FBG coated with NMO is our proposed biosensor.

2. Theoretical Background

2.1. Nanostructure Metal Oxide. NMO materials have great potential as immobilizing matrices for biosensor development [9]. Their use may lead to the fabrication of novel biosensor devices needed to enhance diagnostic. Bruggmann Effective Medium was employed to calculate the effective index of the NMO with the biological liquids or tissues (solid-liquid into and nanobiointerfaces) to fabricate an efficient biosensor. Figure 1 shows many types of NMOs and their biosensing applications [9].

2.2. Bruggmann's Effective Medium Theory. Metal oxide nanostructure material is a composite material with effective index worked out by Bruggmann's effective medium theory

[10, 18]. Bruggmann's approximation starts from Clausius-Mossotti Approximation and involves knowing if a polarizable entity is a sphere of dielectric constant ε_1 and radius a. If so, then elementary electrostatics polarizability is given by [18]

$$\alpha = \frac{(\varepsilon_1 - 1)\, a^3}{(\varepsilon_1 + 2)}, \tag{1}$$

where α is the polarizability.

Substituting the above equation in the following equation:

$$\frac{(\varepsilon - 1)}{(\varepsilon + 2)} = \frac{(4\pi n\alpha)}{3} \tag{2}$$

it yields

$$\frac{\varepsilon - 1}{\varepsilon + 2} = \eta_1 \frac{\varepsilon_1 - 1}{\varepsilon_1 + 2}, \tag{3}$$

where ε is the effective dielectric constant; η_1 is the fraction of space occupied by material with dielectric constant ε_1.

The embedded sphere in a material of dielectric constant ε_0 is then replaced as follows:

$$\frac{\varepsilon - \varepsilon_0}{\varepsilon + 2\varepsilon_0} = \eta_1 \frac{\varepsilon_1 - \varepsilon_0}{\varepsilon_1 + 2\varepsilon_0}. \tag{4}$$

Equation (4) was derived originally from the following equation:

$$\varepsilon - 1 = \frac{4\pi n\alpha E_{\text{eff}}}{E} = \frac{4\pi n\alpha\,(E + 4\pi P/3)}{E} = 4\pi n\alpha \frac{\varepsilon + 2}{3}, \tag{5}$$

where E_{eff} is the effective field as follows [18]:

$$E_{\text{eff}} = E + \left(\frac{4}{3}\right)\pi P, \tag{6}$$

where E is the space average field, P is the polarization which is equal to (np), where n is the number of polarizable entities per unit volume, and p is the induced dipole moment of each.

Bruggmann found that the total polarization summed over the two types of inclusion must vanish; thus,

$$\delta_1 \frac{\sigma_1 - \sigma_m}{\sigma_1 + 2\sigma_m} + \delta_2 \frac{\sigma_2 - \sigma_m}{\sigma_2 + 2\sigma_m} = 0, \tag{7}$$

where σ_1 is the first material conductivity, σ_m is the effective conductivity, σ_2 is the second material conductivity, δ_1 is the first material fraction volume, and δ_2 is the second material fraction volume, $\delta_1 + \delta_2 = 100\%$ or 1. This approximation is the mostly acceptable in this field [18].

3. Tools and Methods

A fiber was coated by a nanostructured TiO_2 followed and then tested by injecting it in some liquids. The procedure is explained in Figure 2.

3D nanostructures TiO_2 were papered by Sol-Gel method, using the following chemicals: Ethanol (CH_3CH_2OH), 7.5 gram

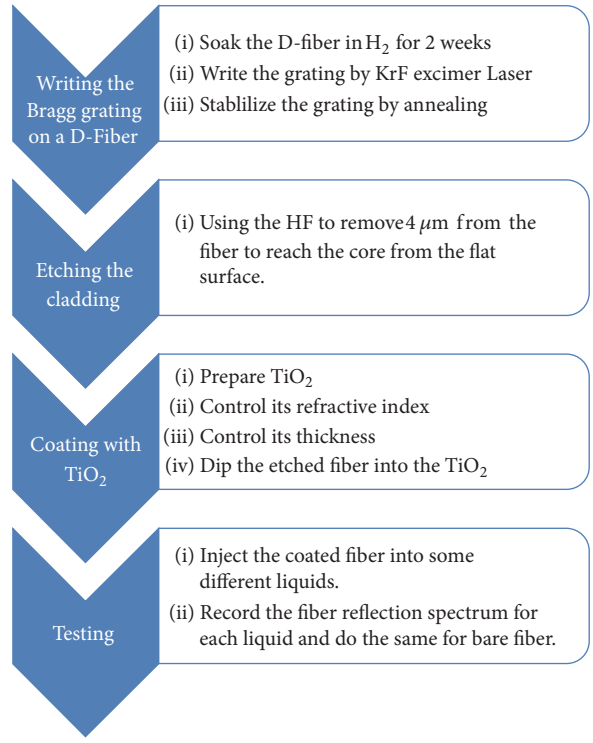

Figure 2: Procedure structure.

(i) Titanium tetrachloride ($TiCl_4$), 0.48 gram

(ii) Hydrochloric acid (HCl), 1.18 gram

(iii) Pluronic-F127, 0.5 gram

Ethanol was mixed, using a stirrer, with drop by drop addition of $TiCl_4$. The weight measurement was continuously taken during mixing. The solution was left at room temperature for a while until reaching ambient temperature. 0.5 gm of Pluronic F-127 was added to the solution while stirring. Hydrochloric acid (HCL) was then added slowly, 2 drops per 30 min, while stirring till the solution turned clear. The PH of the solution was adjusted to 0.5 during stirring and HCl addition. Finally, the solution was stirred for three hours and finally left to set for 24 hours.

3.1. Refractive Index Measurement. 1 cm by 1 cm Thermal Oxide wafer [300 nm SiO_2 layer on Si ($n = 1.455$)] was spin-coated by coater (Headway Research Inc.) with TiO_2 sol-gel. The prepared wafer was placed in a furnace to dry for 2 hours at 60°C. The temperature was made to increase at 3°C/min rate until reaching 120°C and stayed there an hour. Special temperature controller was utilized for this purpose which at the end reached 600°C and held there for 2 hours. Finally, the temperature was decreased by 3°C/min rate until reaching the room temperature at 25°C. Figure 3 shows schematically how the furnace program is run.

To measure the refractive index of the prepared TiO_2 NMO over the wafer, a spectroscopic ellipsometry (HORIBA JOBIN YVOIN) was employed.

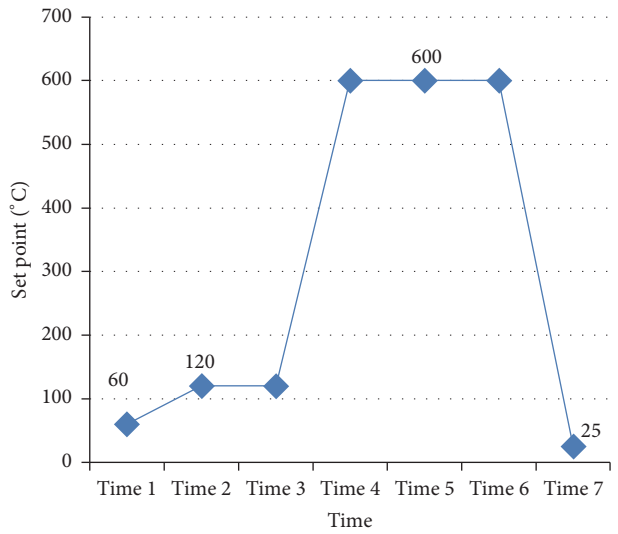

Figure 3: Schematic presentation of the controlled furnace temperature.

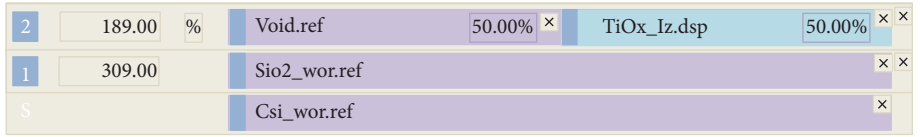

Figure 4: Fitting procedure for the wafer films coated with NMO-TiO_2.

Table 1: Different concentrations of sol-gel preparation for thickness measurements.

Ethanol (g)	$TiCl_4$ (g)	F-127 (g)	HCl (g)
4.5	0.48	0.5	0.7
7.5	0.48	0.5	1.18
9.5	0.48	0.5	1.4
10.5	0.48	0.5	1.42

The samples were fitted as shown in Figure 4, where the wafer film is Si with a 300 nm of SiO_2. This wafer is coated with porous TiO_2 and the third layer is TiO_2 with voids. The voids represent air porosity. The angle of incidence was 70° and the spectrum range is from 400 to 1600 nm by 10 nm increment. The obtained data is shown in Figure 5.

3.2. Thickness Control. Four different TiO_2 Sol-Gels were prepared with different concentrations (Table 1) as a preliminary study to find the suitable thickness over the fiber.

The preparation details are presented in Section 3.1 (TiO_2 NMO preparation method). The 4–6 cm long D-shaped fiber jacket was removed by a fiber-optic stripper and then cleaned by tissue with some ethanol. The D-shaped fiber was dipped into the TiO_2 sol-gel for 20–30 seconds and then dried in the furnace, as explained in Refractive Index Measurement.

JEOL USA JSM-6510LV Scanning Electron Microscope was utilized to measure the thickness of the NMO material on the fiber. Picturing the fiber samples necessitated coating with conducting Palladium ions using CRESSINGTON 108 autosputter coater.

3.2.1. Coating Process. The etched D-shaped fiber was exposed to TiO_2 sol-gel by drawing the fiber at 5 mm/s rate. The fiber was then dried for one day in air and then placed in a furnace following the same program mentioned in Refractive Index Measurement.

Testing the Fabricated FBG-TiO_2. The sensing assembly consists of five main elements. The FBG-TiO_2 NMO was connected from one end to an optical circulator which was connected to a broadband light source type MPB EBS-7210 with a center wavelength of 1565 nm and spectral width of 100 nm at −20 dBm and to Agilent 86140 series optical spectrum analyzer with a wavelength range of 600 nm to 1700 nm and accuracy of ±0.01 nm for 1480 to 1570 nm. The FBG-TiO_2 NMO was placed in a glass tube; then deionized water and saline were injected into this tube for sensing. The assembly is shown in Figure 6.

The Bragg wavelength was recorded in air, deionized water, and saline. To ensure that the prepared FBG-TiO_2 NMO was better than that without NMO coating, the etched

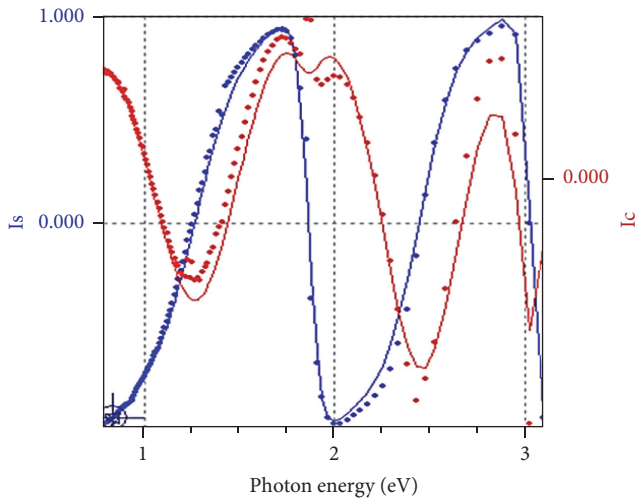

Figure 5: Spectroscopic ellipsometry data fitting procedure of TiO_2 NMO.

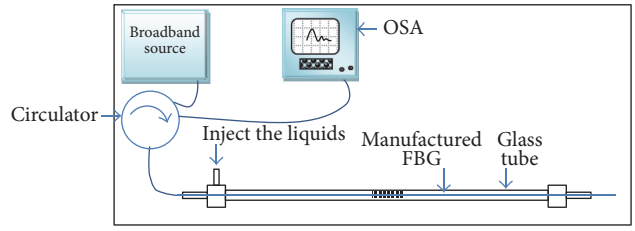

Figure 6: Reflection spectrum measurement by a D-shaped FBG with TiO_2.

D-shaped FBG was used in the same assembly to record the Bragg wavelength for air, deionized water, and saline.

4. Results

4.1. Spectroscopic Ellipsometry Refractive Index Results. The refractive index of the coated TiO_2 NMO on a thin film was measured as a function of the incident wavelengths and found to be 1.487 at 1550 nm, Figure 7.

4.2. Scanning Electron Microscope Thickness Results. The theoretical value of the coated TiO_2 NMO thickness over the D-shaped fiber was deduced from the results published by Poole et al. of which Comsol multiphysics simulation was applied [10, 19]. Their work was done for tin dioxide (SnO_2) as shown in Figure 8. The figure gives a combined refractive index and losses percentage for a given set of thicknesses. In our experiment, the desired 1.6 effective refractive index requires thicknesses that may range between 200 nm and 300 nm taking into account the difference in the optical properties of the TiO_2 and SnO_2. Nevertheless this refractive index does not satisfy the guiding condition of light through the fiber; so a control on the thickness of the coated NMO was needed. This thickness should keep the radiation modes of light beam propagating inside the optical fiber when it is dipped in the postulated solutions.

Many TiO_2 sol-gel samples for coating the fiber were prepared and examined by SEM to find the suitable concentration of the TiO_2 to sense saline.

Figures 9(a) and 9(b) show the SEM images for 4 prepared coated D-shaped optical fibers.

For (9 : 0.96 : 1 : 1.4) g ratio of ethanol : $TiCl_4$: F-127 : HCl of TiO_2 NMO coating over the optical fiber gave a thickness of about 339 nm. The ethanol concentration was increased by 65% of its first value, and the second ethanol : $TiCl_4$: F-127 : HCl (15 : 0.96 : 1 : 2.36) g ratio of TiO_2 NMO coating over the optical fiber gave a thickness of about 312 nm. The ethanol concentration was then increased by 25% of its second value, and the third ethanol : $TiCl_4$: F-127 : HCl (19 : 0.96 : 1 : 2.8) g ratio of TiO_2 NMO coating over the optical fiber gave a thickness of about 244 nm.

The ethanol concentration was finally increased by 10% of its third value, and the fourth ethanol : $TiCl_4$: F-127 : HCl (21 : 0.96 : 1 : 2.84) g ratio of TiO_2 NMO coating over the optical fiber resulted in a thickness of about 207 nm.

Figure 11 shows a relationship between ethanol concentrations and the resultant thickness of the TiO_2 NMO coating over the D-shaped optical fiber. From these results and Figure 9, the best TiO_2 sol-gel concentration was the second one.

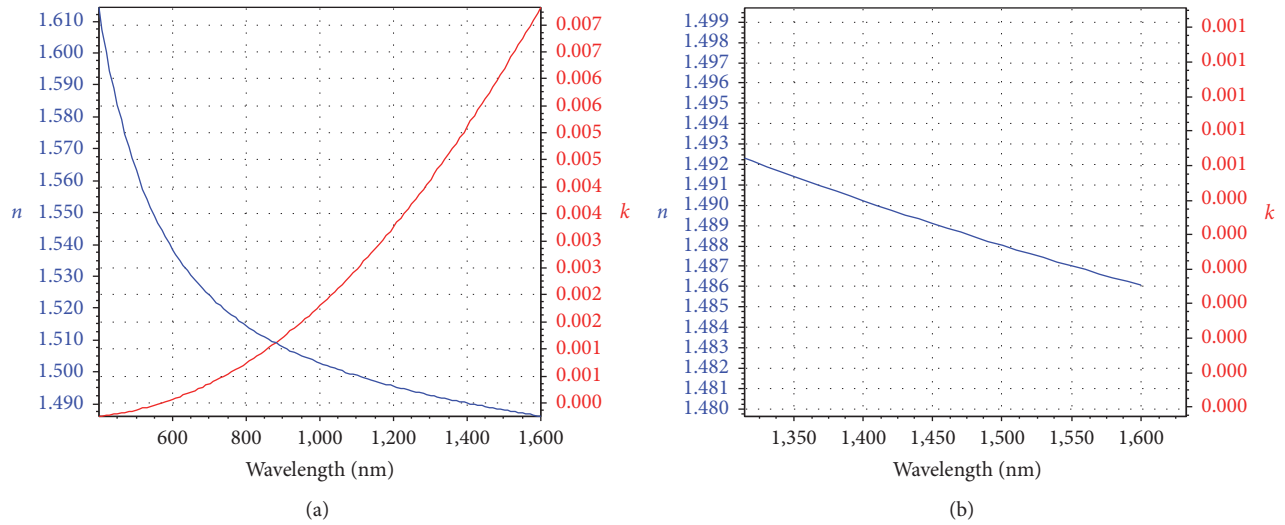

FIGURE 7: (a) The refractive index (real part (n) and imaginary part (k)) of TiO_2 NMO as a function of the incident wavelength as a result from the spectroscopic ellipsometry for the sample prepared in Section 3.1 (TiO_2 NMO preparation method). (b) Magnification of the real part of the refractive index of TiO_2 NMO.

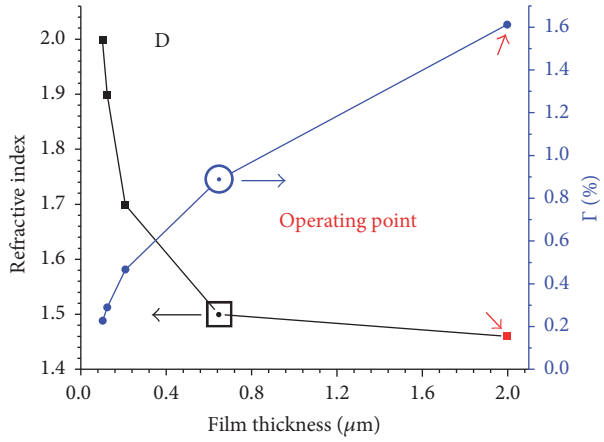

FIGURE 8: The relation between the effective refractive index of NMO-SnO_2 and its thickness on the optical fiber [10].

4.3. Assembly Results with a Bare FBG. The etched D-shaped FBG sensing ability was tested as shown in Figure 9. The reflection spectrum was recorded and presented in Figure 11. The black line refers to the FBG in air and the green line refers to the same sample but dipped in deionized water. It is obvious from this figure that there is a slight shift in the Bragg wavelength due to the difference in refractive index between air ($n = 1$, $\lambda_{Bragg} = 1549.8$ nm) and deionized water ($n = 1.318$, $\lambda_{Bragg} = 1549.9$ nm) so the wavelength shift $\Delta\lambda_{Bragg}$ is 0.1 nm. The sensitivity (ratio between the Bragg wavelength shift and the difference in the surrounding index, $\Delta n_{surrounding} = 0.318$) was deduced and found to be 0.3144 nm/riu.

The deionized water was replaced by saline water. The same measurements were recorded and the resultant reflectivity spectrum was recorded as shown in Figure 12, where the reflection spectrum recorded (the black line) refers to the FBG in air $\lambda_{Bragg} = 1549.8$ nm and the green line refers to the same sample but dipped in saline water $\lambda_{Bragg} = 1549.75$ nm. It is obvious from this figure that there is a very slight shift of 0.05 nm in the Bragg wavelength. The sensitivity was 0.142 nm/riu.

4.4. Assembly Results with FBG-TiO_2 NMO. The etched D-shaped FBG was coated with ethanol : $TiCl_4$: F-127 : HCl at 15 : 0.96 : 1 : 2.36 g ratio of TiO_2 sol-gel and dried at the ambient temperature for 24 hours. The sample was used in the assembly shown in Figure 6 to test its sensing ability. The reflection spectrum was recorded in air as shown in Figure 13 (black line, $\lambda_{Bragg} = 1549.8$ nm). The measurement was repeated after dipping in a deionized water and the resultant

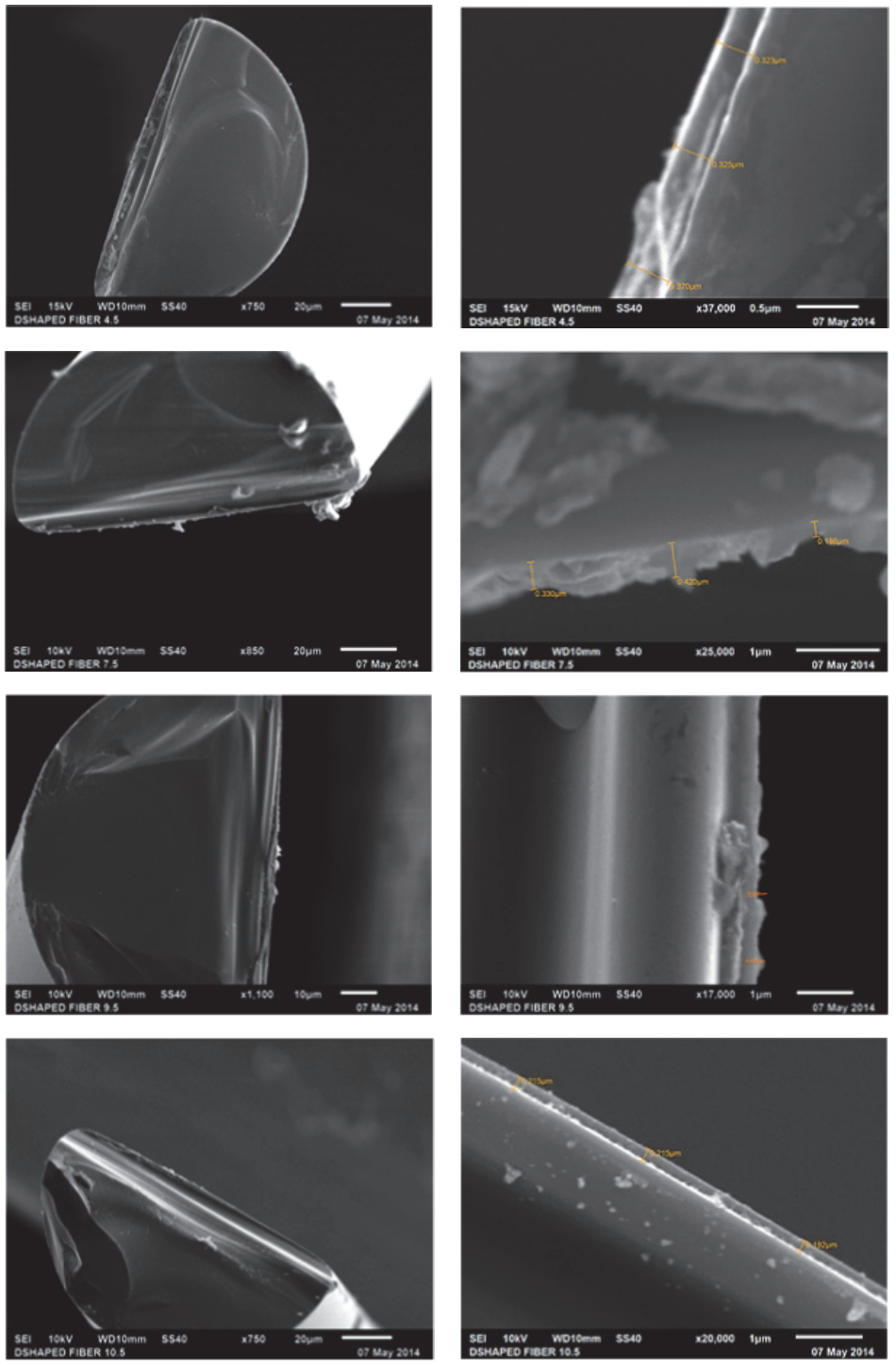

(a) (b)

FIGURE 9: The SEM pictures of the D-shaped fiber coated with nanostructured metal oxide material (TiO_2). (a) is an amplified image of (b). The mean values of the resultant thickness measurement are shown in Figure 10.

reflection spectrum is shown in Figure 13, (green line, λ_{Bragg} = 1549.4 nm). The obtained sensitivity was 1.257 nm/riu.

The deionized water was then replaced by saline water. The same measurements were recorded and the resultant reflectivity spectrum was recorded as shown in Figure 14.

The reflectivity spectrum of the TiO_2 NMO coated FBG in air is in a black line with λ_{Bragg} = 1549.8 nm and the reflectivity spectrum of the same sample but in saline water is in a green line with λ_{Bragg} = 1549.5 nm. The sensitivity is 0.857 nm/riu.

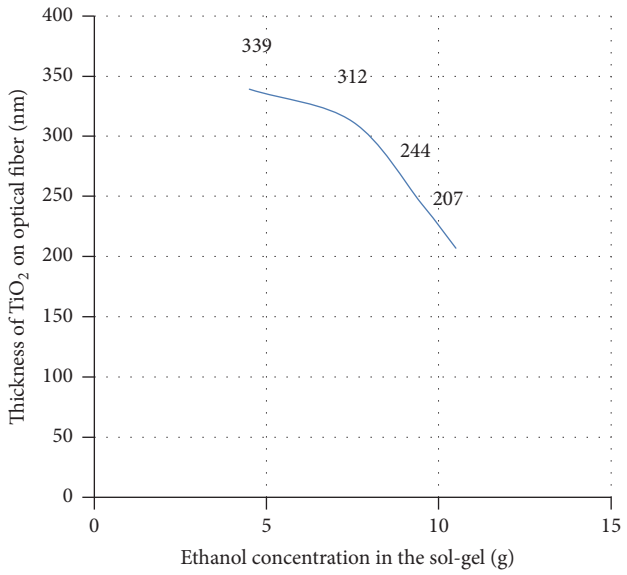

Figure 10: The relation between the different concentrations of ethanol in the sol-gel to the thickness of the TiO_2 on the optical fiber.

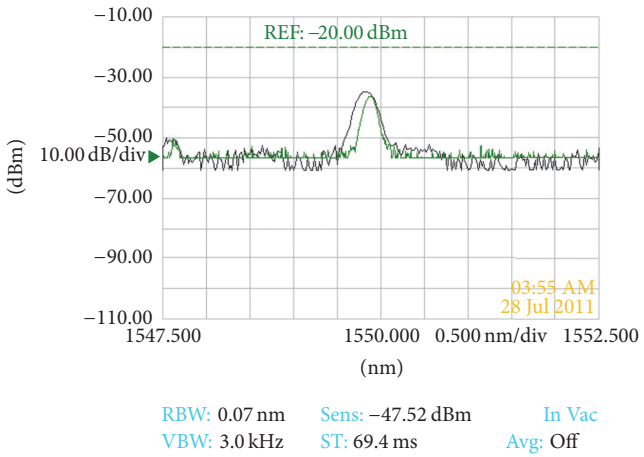

Figure 11: The reflectivity spectrum of the etched-FBG in the air (black line) and the reflectivity spectrum of the same FBG in the deionized water (green line).

5. Conclusion

Higher shifts and narrower peaks in the Bragg wavelength were obtained after coating the fiber with few hundreds nanometers' thick TiO_2 NMO of 20 nm–50 nm hole diameters. The sensitivity of the FBG with the TiO_2 NMO is higher than that without coating due to the nanostructure large surface area. The detected sensitivity was 1.257 nm/riu for air-deionized water and 0.857 nm/riu for air-saline. It is reasonable to be effectively low cost biosensor.

Competing Interests

The authors declare that they have no competing interests.

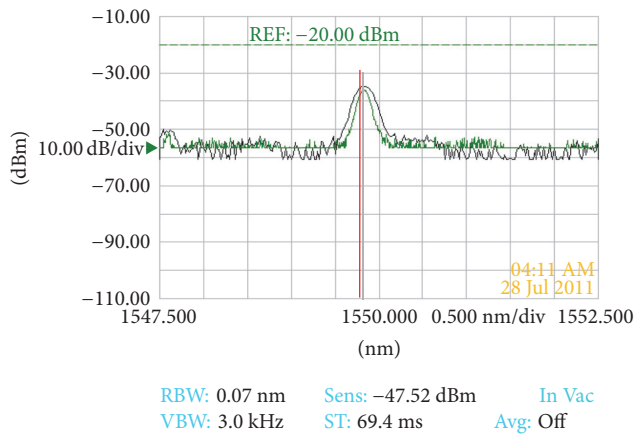

Figure 12: The reflectivity spectrum of the etched-FBG in the air (black line) and the reflectivity spectrum of the same FBG in the saline water (green line).

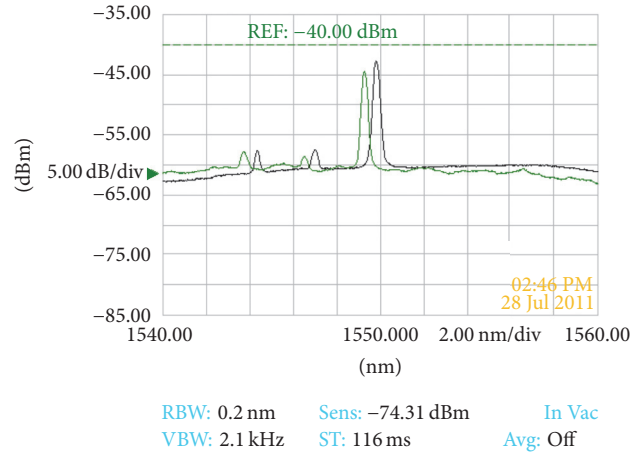

Figure 13: The reflectivity spectrum of the etched-FBG coated with TiO_2 NMO in the air (black line) and the reflectivity spectrum of the same FBG in the deionized water (green line).

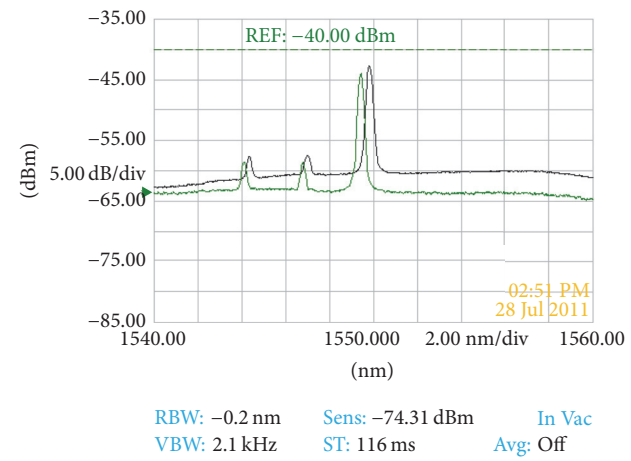

Figure 14: The reflectivity spectrum of the etched-FBG coated with TiO_2 NMO in the air (black line) and the reflectivity spectrum of the same FBG in the saline water (green line).

References

[1] A. Swanton, D. J. Armes, K. J. Young-Smith, C. Dix, and R. Kashyap, "Use of e-beam written, reactive ion etched, phase masks for the generation of novel photorefractive fibre gratings," *Microelectronic Engineering*, vol. 30, no. 1–4, pp. 509–512, 1996.

[2] P. J. Lemaire, R. M. Atkins, V. Mizrahi, and W. A. Reed, "High pressure H_2 loading as a technique for achieving ultrahigh UV photosensitivity and thermal sensitivity in GeO_2 doped optical fibres," *Electronics Letters*, vol. 29, no. 13, pp. 1191–1193, 1993.

[3] K. Zhou, X. Chen, L. Zhang, and I. Bennion, "High-sensitivity optical chemsensor based on etched D-fibre Bragg gratings," *Electronics Letters*, vol. 40, no. 4, pp. 232–234, 2004.

[4] S. Korposh, S.-W. Lee, S. W. James, and R. P. Tatam, "Refractive index sensitivity of fibre-optic long period gratings coated with SiO2 nanoparticle mesoporous thin films," *Measurement Science and Technology*, vol. 22, no. 7, Article ID 075208, 2011.

[5] A. Cusano, P. Pilla, L. Contessa et al., "High-sensitivity optical chemosensor based on coated long-period gratings for sub-ppm chemical detection in water," *Applied Physics Letters*, vol. 87, no. 23, Article ID 234105, pp. 1–3, 2005.

[6] J. F. Akki, A. S. Lalasangi, K. G. Manohar, P. Raikar, T. Srinivas, and U. S. Raikar, "Detection and determination of manganese concentration in water using a fiber Bragg grating coupled with nanotechnology," *Applied Optics*, vol. 50, no. 32, pp. 6033–6038, 2011.

[7] P. T. Arasu, A. S. M. Noor, A. A. Shabaneh et al., "Absorbance properties of gold coated fiber Bragg grating sensor for aqueous ethanol," *Journal of the European Optical Society*, vol. 9, article no. 14018, 2014.

[8] A. G. Mantzila and M. I. Prodromidis, "Development and study of anodic Ti/TiO_2 electrodes and their potential use as impedimetric immunosensors," *Electrochimica Acta*, vol. 51, no. 17, pp. 3537–3542, 2006.

[9] P. R. Solanki, A. Kaushik, V. V. Agrawal, and B. D. Malhotra, "Nanostructured metal oxide-based biosensors," *NPG Asia Materials*, vol. 3, no. 1, pp. 17–24, 2011.

[10] Z. L. Poole, P. Ohodnicki, R. Chen, Y. Lin, and K. P. Chen, "Engineering metal oxide nanostructures for the fiber optic sensor platform," *Optics Express*, vol. 22, no. 3, pp. 2665–2674, 2014.

[11] E. Davies, R. Viitala, M. Salomäki, S. Areva, L. Zhang, and I. Bennion, "Sol–gel derived coating applied to long-period gratings for enhanced refractive index sensing properties," *Journal of Optics A: Pure and Applied Optics*, vol. 11, no. 1, 2009.

[12] K.-S. Mun, S. D. Alvarez, W.-Y. Choi, and M. J. Sailor, "A stable, label-free optical interferometric biosensor based on TiO_2 nanotube arrays," *ACS Nano*, vol. 4, no. 4, pp. 2070–2076, 2010.

[13] R. Liang, Q. Sun, J. Wo, and D. Liu, "Theoretical investigation on refractive index sensor based on Bragg grating in micro/nanofiber," in *Proceedings of the Symposium on Photonics and Optoelectronics (SOPO '11)*, Wuhan, China, May 2011.

[14] M. Smietana, W. J. Bock, and P. Mikulic, "Temperature sensitivity of silicon nitride nanocoated long-period gratings working in various surrounding media," *Measurement Science and Technology*, vol. 22, no. 11, Article ID 115203, 2011.

[15] T. Chen, *Fiber optic sensors for extreme environments [Ph.D. thesis]*, University of Pittsburgh, Swanson School of Engineering, 2012.

[16] X. Zhang, H. Alemohammad, and E. Toyserkani, "Sensitivity alteration of fiber Bragg grating sensors with additive micro-scale bi-material coatings," *Measurement Science and Technology*, vol. 24, no. 2, 2013.

[17] S. C. M. Ho, L. Ren, H.-N. Li, and G. Song, "A fiber Bragg grating sensor for detection of liquid water in concrete structures," *Smart Materials and Structures*, vol. 22, no. 5, Article ID 055012, 2013.

[18] R. Landauer, "Electrical conductivity in inhomogeneous media," *AIP Conference Proceedings*, vol. 40, pp. 2–45, 1978.

[19] Z. L. Poole, P. Ohodnicki, M. Buric et al., "Block copolymer assisted refractive index engineering of metal oxides for applications in optical sensing," in *Nanophotonic Materials XI*, vol. 9161, San Diego, Calif, USA, August 2014.

Hindawi
Journal of Nanotechnology
Volume 2017, Article ID 5104841, 4 pages
https://doi.org/10.1155/2017/5104841

Research Article

Controllable Growth of the ZnO Nanorod Arrays on the Al Substrate and Their Reversible Wettability Transition

Hong Li,[1] Hongyan Liu,[2] Yushan Li,[2] and Qinzhuang Liu[1]

[1]*School of Physics and Electronic Information, Huaibei Normal University, Huaibei 235000, China*
[2]*Department of Physics, Heze University, Heze 274015, China*

Correspondence should be addressed to Qinzhuang Liu; qzliu@mail.ustc.edu.cn

Received 8 December 2016; Accepted 17 January 2017; Published 23 February 2017

Academic Editor: Paresh Chandra Ray

Copyright © 2017 Hong Li et al. This is an open access article distributed under the Creative Commons Attribution License, which permits unrestricted use, distribution, and reproduction in any medium, provided the original work is properly cited.

High-quality ZnO nanorod arrays are formed using the ZnO nanoflakes on the Al substrate as seed layer. A reversible wettability transition can be easily achieved via alternation of UV irradiation and dark storage. The physical adsorption of the water molecules on the surface of ZnO nanorod arrays is considered to be responsible for this transition, which is confirmed by X-ray photoelectron spectroscopy.

1. Introduction

Wettability design and manipulation have received particular attention in modern society because of its potential applications [1–3]. Wettability results from low surface free energy and surface morphology with special micro- and nanorough structures [4, 5]. Recently, with the rapid development of the smart devices, such as intelligent small droplet manipulation, reversible wettability switch has become a research focus and been realized by modification of responsive materials [6]. Such responsive materials present intrinsic reaction when they face the different environmental stimuli such as light illumination [7], pH [8], electric field [9], and temperature [10]. Being a photoresponsive semiconductor, the ZnO has aroused great attention because of its special electronic, optical, and acoustic properties [11]. Reversible wettability switch on the solid surface modified by ZnO nanostructure has been reported [12]. Reversible superhydrophobicity to superhydrophilicity switch was observed on the glass wafer coated by ZnO nanorods [13].

In this paper, high-quality ZnO nanorod arrays are achieved by hydrothermal and chemical vapor deposition route on the Al substrate. The wettability transition between the superhydrophobicity and superhydrophilicity is observed via alternation of UV irradiation and dark storage. The nanostructure and special photoelectric properties of the ZnO are two important factors for the wettability transition.

2. Methods

The procedure to growing high-quality vertical ZnO nanorod arrays consists of two steps: (1) growing two-dimensional ZnO nanoflakes on the Al substrates using low-temperature hydrothermal route and (2) the formation of high-quality vertical ZnO nanorod arrays on the surface of two-dimensional ZnO nanoflakes through chemical vapor deposition route.

In the first step, Al substrate was cleaned thoroughly in acetone for about 30 min by ultrasonic waves and cleaned with deionized water in sequence. The Al substrate was suspended in the beaker filled with aqueous solution of zinc nitrate hydrate (8 mM) and hexamethylenetetramine (8 mM) at 95°C for 2 h. The Al substrate was then taken out from the solution, rinsed with deionized water, and dried by a nitrogen stream. Last, the sample was annealed at 450°C in air for 30 min.

In the second step, the alumina boat with Zn powder (purity: 99.999%) was placed into the horizontal tube furnace. The sample which was prepared in the first step was put horizontally on the downstream side of the alumina boat at a distance of 8 cm. Before the growth, argon was introduced

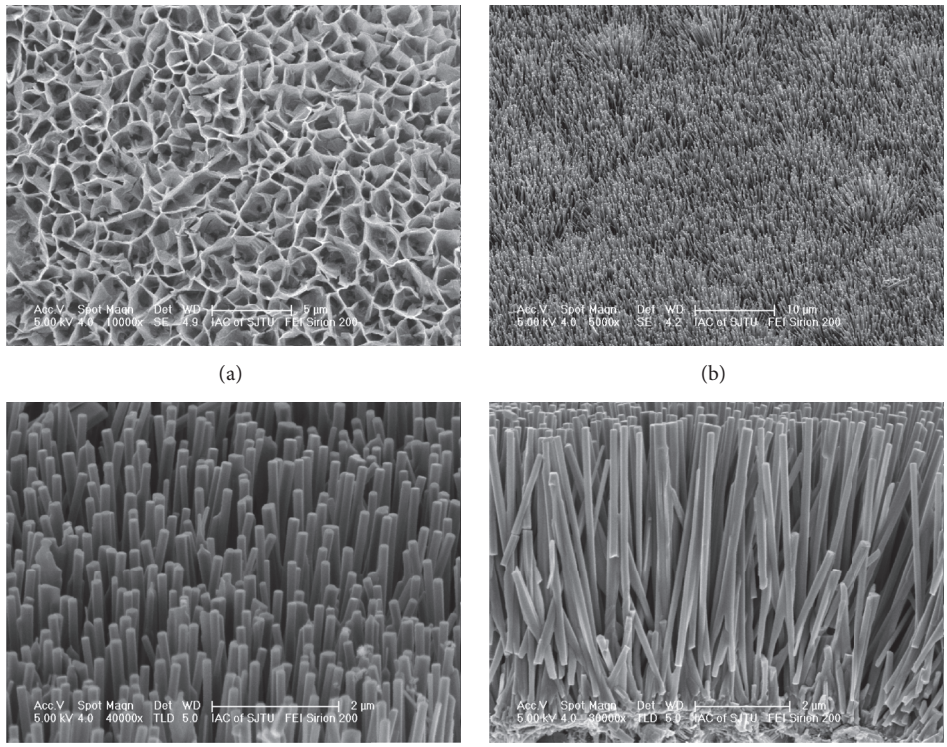

Figure 1: SEM images of the as-grown ZnO samples on the Al substrate. (a) Large-area view of the ZnO nanoflakes on the Al substrate, (b) top images of the ZnO nanorod arrays and (c) high magnification ZnO nanorod arrays, and (d) side views of the ZnO nanorod arrays.

into the system through a mass-flow controller with a flow 120 sccm and the pressure was maintained at 80 Pa. The temperature of the furnace was changed linearly with time to 600°C at the rate of 20°C/min. Subsequently, oxygen was given to the system at a flow rate of 100 sccm. The reaction was carried out at about 600°C for 40 min. After that, the furnace was cooled to room temperature, while argon and oxygen flow was stopped. The as-grown film was stored in the dark environment for a week before being measured.

The morphologies of sample nanostructure were characterized by scanning electron microscopy (SEM, Philips Sirion 200). The component of the sample was characterized by X-ray diffraction (XRD, D/max-2200/PC). The water contact angles (WCAs) on the surface were measured with deionized water of 5 μl by using an optical contact angle meter system at ambient temperature (Data Physics Instrument GmbH, Germany). The X-ray photoelectron spectroscopy spectrum (XPS) of the samples was measured by Thermo ESCALAB 250.

3. Results and Discussions

Figure 1(a) shows the typical morphology of ZnO nanoflakes on the Al substrate using low-temperature hydrothermal route. Many sheet-like ZnO nanoflakes were produced and nearly vertical to the Al substrate. Figure 1(b) is image of the ZnO nanorod arrays coated on the ZnO nanoflakes. Figure 1(c) is the further magnified image. From the SEM image as showed in Figure 1(c), the ZnO nanorod arrays have a flat surface morphology, with almost the same diameters of about 150 nm. Side image of the SEM view of the arrays (Figure 1(d)) suggests that the ZnO nanorod arrays grow completely vertically and the height is about 5 μm. Figure 2 compared the XRD spectrum of the ZnO nanorod arrays (Figure 2(a)) with the ZnO nanoflakes (Figure 2(b)) on the Al substrate. The XRD spectrum of the ZnO nanorod arrays is almost the same as the ZnO nanoflakes, indicating that the orientation of the ZnO nanoflakes is of great importance to the orientation of the ZnO nanorod arrays. It is well-known that the effect of seeds layer is very important in fabricating high-quality vertical ZnO nanorod arrays. So we can deduce that the role of ZnO nanoflakes on the Al substrate is seeding which directly leads to the formation of ZnO nanorod arrays.

The wettability of the ZnO nanorod arrays is studied by water contact angle (WCA) measurement. The WCA on the surface coated by ZnO nanorod arrays is about 158° as shown in Figure 3(a). After UV illumination, the WCA is about 0°. After depositing the film which was irradiated by the UV in the dark environment for five days, the film is still superhydrophobic again. This process can be repeated many times and the corresponding process is shown in Figure 4.

Surface free energy and surface morphology have important effects on the surface wettability. The high-quality ZnO nanorod arrays on the Al substrate in Figure 1 increase the air

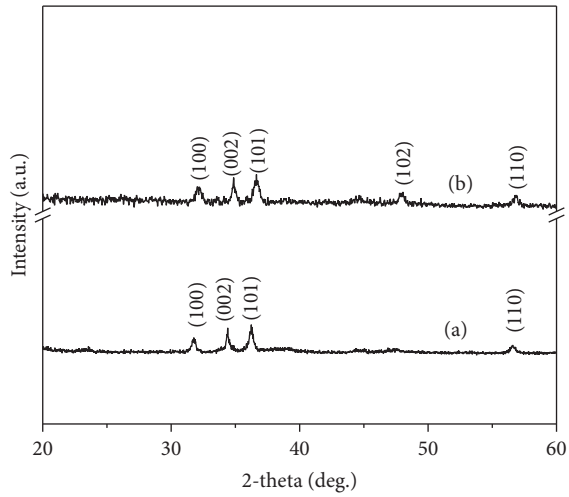

Figure 2: XRD patterns of the as-grown ZnO samples. (a) ZnO nanorod arrays. (b) ZnO nanoflakes.

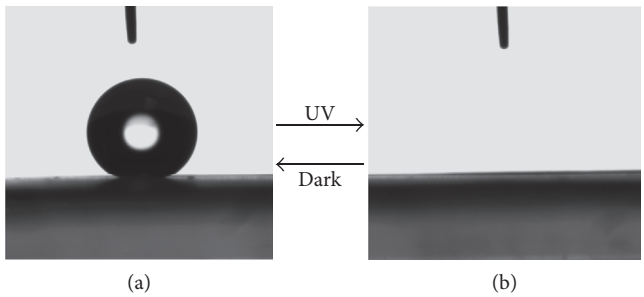

Figure 3: The shape of water droplet on the ZnO nanorod arrays (a) before UV irradiation and (b) after UV irradiation.

fraction of the water-air interface. This means that the special nanostructure will increase the WCA. The superhydrophobicity of the ZnO nanorod arrays can be explained by Cassie equation [14]:

$$\cos\theta^* = -1 + f_1 (1 + \cos\theta), \quad (1)$$

where θ^* and θ are CA on the rough and flat surface and f_1 is the solid fraction in contact with water. Because the surface roughness of ZnO nanorod arrays is much higher than ZnO nanoflakes, much air is easy blocked among the ZnO nanorod arrays when the water droplet is placed on it, so the value of f_1 decreases rapidly and the CA increases. This is the reason that the Al substrate coated by ZnO nanorod arrays shows superhydrophobicity.

The wettability of the solid is determined by surface free energy and the geometric structure. The geometric structures of the ZnO nanorod arrays do not change before and after UV irradiation, indicating that the wettability transition is caused by surface free energy. Hole of electron-hole pairs generated in the ZnO by UV irradiation will react with lattice oxygen to form surface oxygen vacancies [15, 16]. Subsequently, water molecules absorbed at the surface oxygen vacancies will produce the hydroxyl groups which lead to the physical adsorption of the water molecules. The hydrophilicity of film

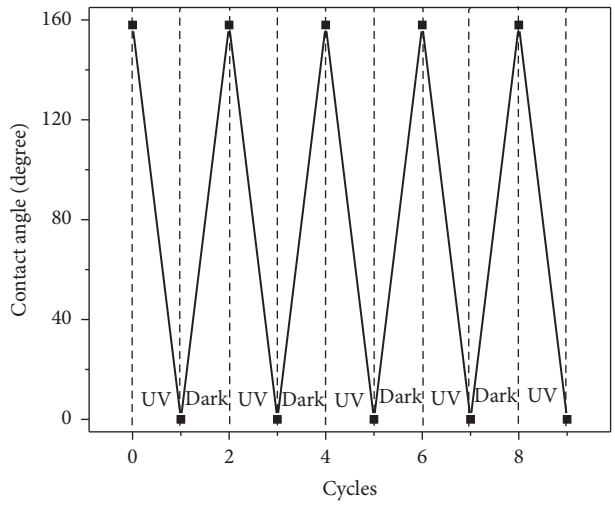

Figure 4: Reversible wettability switching by alternating UV irradiation and dark storage.

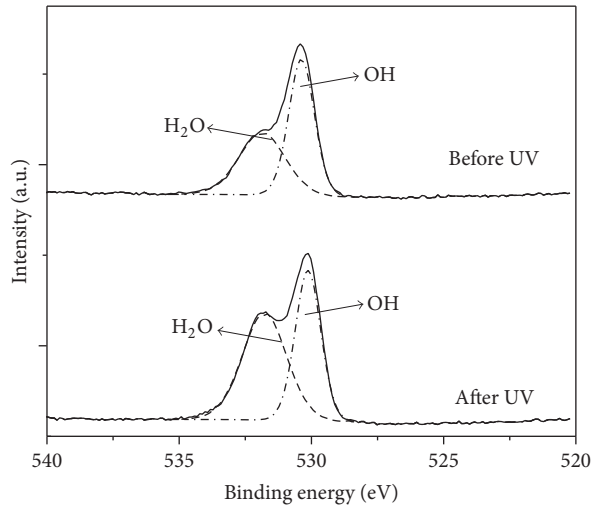

Figure 5: X-ray photoelectron spectroscopy spectra of the O 1s level before and after UV irradiation.

increases. Figure 5 shows the XPS of ZnO nanorod arrays before and after UV irradiation. The shoulder and intensity of the O 1s at the higher binding energy are increased. This confirms the existence of physical adsorption of the water molecules on the surface of ZnO nanorod arrays. From Wenzel equation [17],

$$\cos\theta^* = r\cos\theta, \quad (2)$$

where r is rough factor and the hydrophilicity of film will be enhanced to superhydrophilicity because of the special nanostructure. Oxygen atoms gradually take the place of the hydroxyl groups adsorbed on the ZnO nanorod arrays when the film was placed in the dark. In the end, the surface wettability changes back to the superhydrophobicity.

In order to acquire the detailed information about the effect of UV illumination on the WCA, Figure 6 has given the WCA as the function of UV illumination time. It can be seen

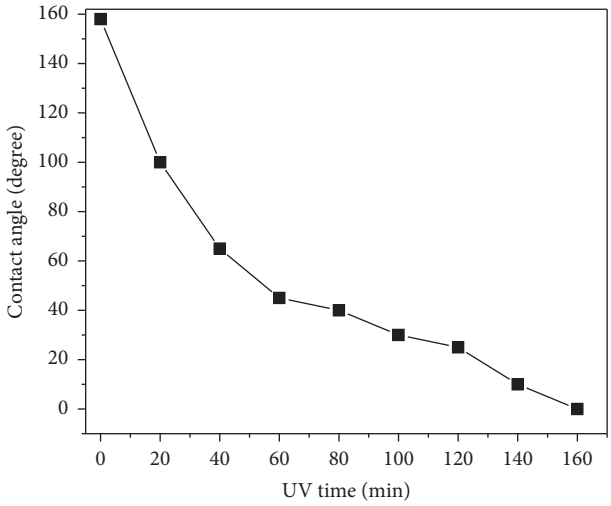

Figure 6: Contact angle versus UV irradiation time for the water droplet on the surface of ZnO nanorod arrays.

that the WCA decreases abruptly from 158° to 50° about after 60 min of UV irradiation because of the high speed yielding of electron-hole pairs after UV irradiation. With the increase of illumination time from 60 to 160 min, the change speed of WCA is slow and, at last, the wettability of film changes from superhydrophobicity to superhydrophilicity.

4. Conclusions

Dense and vertically aligned ZnO nanorod arrays with a large area are fabricated by a simple two-step process on the Al substrate. The as-grown film shows good superhydrophobicity and the contact angle is about 158°. The film shows good superhydrophilicity and the contact angle is about 0° after UV irradiation. Reversible wettability transition is achieved via alternation of UV irradiation and dark storage. The nanostructure and special photoelectric properties of the ZnO are two important factors for this behavior.

Competing Interests

The authors declare that there is no conflict of interests regarding the publication of this paper.

Acknowledgments

This work was supported by Natural Science Foundation of Anhui Province (no. 1408085QA19) and Natural Science General Foundation of Anhui Higher Education Institutions of China (no. KJ2014B03).

References

[1] L. Feng, Z. Zhang, Z. Mai et al., "A super-hydrophobic and super-oleophilic coating mesh film for the separation of oil and water," *Angewandte Chemie - International Edition*, vol. 43, no. 15, pp. 2012–2014, 2004.

[2] T. Sun, L. Feng, X. Gao, and L. Jiang, "Bioinspired surfaces with special wettability," *Accounts of Chemical Research*, vol. 38, no. 8, pp. 644–652, 2005.

[3] X. Feng and L. Jiang, "Design and creation of superwetting/antiwetting surfaces," *Advanced Materials*, vol. 18, no. 23, pp. 3063–3078, 2006.

[4] B. K. Nayak, P. O. Caffrey, C. R. Speck, and M. C. Gupta, "Superhydrophobic surfaces by replication of micro/nanostructures fabricated by ultrafast-laser-microtexturing," *Applied Surface Science*, vol. 266, pp. 27–32, 2013.

[5] Y. Coffinier, S. Janel, A. Addad et al., "Preparation of superhydrophobic silicon oxide nanowire surfaces," *Langmuir*, vol. 23, no. 4, pp. 1608–1611, 2007.

[6] W. Li, T. Guo, T. Meng et al., "Enhanced reversible wettability conversion of micro-nano hierarchical TiO_2/SiO_2 composite films under UV irradiation," *Applied Surface Science*, vol. 283, pp. 12–18, 2013.

[7] H. Liu, L. Feng, J. Zhai, L. Jiang, and D. Zhu, "Reversible wettability of a chemical vapor deposition prepared ZnO film between superhydrophobicity and superhydrophilicity," *Langmuir*, vol. 20, no. 14, pp. 5659–5661, 2004.

[8] X. Yu, Z. Wang, Y. Jiang, F. Shi, and X. Zhang, "Reversible pH-responsive surface: from superhydrophobicity to superhydrophilicity," *Advanced Materials*, vol. 17, no. 10, pp. 1289–1293, 2005.

[9] B. Kakade, R. Mehta, A. Durge, S. Kulkarni, and V. Pillai, "Electric field induced, superhydrophobic to superhydrophilic switching in multiwalled carbon nanotube papers," *Nano Letters*, vol. 8, no. 9, pp. 2693–2696, 2008.

[10] B. Xue, L. Gao, Y. Hou, Z. Liu, and L. Jiang, "Temperature controlled water/oil wettability of a surface fabricated by a block copolymer: application as a dual water/oil on-off switch," *Advanced Materials*, vol. 25, no. 2, pp. 273–277, 2013.

[11] J. Lü, K. Huang, X. Chen et al., "Reversible wettability of nanostructured ZnO thin films by sol-gel method," *Applied Surface Science*, vol. 256, no. 14, pp. 4720–4723, 2010.

[12] H. Li, M. J. Zheng, S. D. Liu, L. Ma, C. Q. Zhu, and Z. Z. Xiong, "Reversible surface wettability transition between superhydrophobicity and superhydrophilicity on hierarchical micro/nanostructure ZnO mesh films," *Surface and Coatings Technology*, vol. 224, pp. 88–92, 2013.

[13] X. Feng, L. Feng, M. Jin, J. Zhai, L. Jiang, and D. Zhu, "Reversible super-hydrophobicity to super-hydrophilicity transition of aligned ZnO nanorod films," *Journal of the American Chemical Society*, vol. 126, no. 1, pp. 62–63, 2004.

[14] A. B. D. Cassie and S. Baxter, "Wettability of porous surfaces," *Transactions of the Faraday Society*, vol. 40, pp. 546–551, 1944.

[15] W. H. Hirschwald, "Zinc oxide: an outstanding example of a binary compound semiconductor," *Accounts of Chemical Research*, vol. 18, no. 8, pp. 228–234, 1985.

[16] M. Miyauchi, A. Nakajima, A. Fujishima, K. Hashimoto, and T. Watanabe, "Photoinduced surface reaction on TiO_2 and $SrTiO_3$ films: photocatalytic oxidation and photoinduced hydrophilicity," *Chemistry of Materials*, vol. 12, no. 1, pp. 3–5, 2000.

[17] R. N. Wenzel, "Resistance of solid surfaces to wetting by water," *Industrial & Engineering Chemistry*, vol. 28, no. 8, pp. 988–994, 1936.

Hindawi
Journal of Nanotechnology
Volume 2017, Article ID 6987430, 6 pages
https://doi.org/10.1155/2017/6987430

Research Article

Effect of Vacancy Defects on the Electronic Structure and Optical Properties of GaN

Lili Cai and Cuiju Feng

Foundation Department, North China Institute of Science and Technology, Beijing 101601, China

Correspondence should be addressed to Lili Cai; lily2004c@163.com

Received 20 November 2016; Accepted 12 January 2017; Published 12 February 2017

Academic Editor: Yongxing Zhang

Copyright © 2017 Lili Cai and Cuiju Feng. This is an open access article distributed under the Creative Commons Attribution License, which permits unrestricted use, distribution, and reproduction in any medium, provided the original work is properly cited.

The effect of gallium vacancy (V_{Ga}) and nitrogen vacancy (V_N) defects on the electronic structure and optical properties of GaN using the generalized gradient approximation method within the density functional theory were investigated. The results show that the band gap increases in GaN with vacancy defects. Crystal parameters decrease in GaN with nitrogen vacancy (GaN:V_N) and increase in GaN with gallium vacancy (GaN:V_{Ga}). The Ga vacancy introduces defect levels at the top of the valence band, and the defect levels are contributed by N2p electron states. In addition, the energy band shifts to lower energy in GaN:V_N and moves to higher energy in GaN:V_{Ga}. The level splitting is observed in the N2p states of GaN:V_N and Ga3d states of GaN:V_{Ga}. New peaks appear in lower energy region of imaginary dielectric function in GaN:V_N and GaN:V_{Ga}. The main peak moves to higher energy slightly and the intensity decreases.

1. Introduction

GaN is so called third generation semiconductor materials with wide band gap. With the rapid developments of semiconductor technology, it has become the research focus in semiconductor materials in past decades. The band gap of GaN is 3.39 eV at room temperature. Particularly, the GaN-based materials have the advantages of wide band gap, fast electron drift velocity, high temperature resistance, high pressure tolerance, and antiradiation [1]. So they have attracted much attention in the preparation of short wavelength luminescence device and high power microwave device. GaN is the core material and basic device of the new semiconductor optoelectronics industry. The defects and impurities in GaN have a great influence on the electron transport and optical properties of materials. Simulation is a good method to study defects in semiconductor materials except experiment. There is a lot of research on GaN used experiment or theoretical calculation [2–4]. Neugebauer and Van De Walle calculated the electronic structure and atomic structure of the intrinsic defects of GaN by first principles [5]. Boguslawski et al. simulated the intrinsic defects of GaN using ab initio molecular dynamics [6]. Kang et al. calculated the defects in GaN epitaxial layer by first principles. It is believed that C, O impurity and intrinsic defects may be the sources of yellow and blue light [7]. Shen and Kang studied the intrinsic defects of six-party GaN and the electronic structure of C and O using local density functional theory [8]. These methods are based on first principles to calculate the formation energy of GaN and the electronic structure of C and O. In this paper, we studied the effect of V_{Ga} and V_N on the electronic structure and optical properties of GaN using first principles.

2. Model and Calculation

Pure GaN is hexahedron wurtzite structure. It belongs to P63mc space group. Its symmetry is $C_{6v\text{-}4}$. The lattice constants are $a = b = 0.3189$ nm, $c = 0.5185$ nm, $\alpha = \beta = 90^\circ$, and $\gamma = 120^\circ$. c/a is 1.626. It is slightly smaller than the ideal hexagonal close packed structure of 1.633. Figure 1(a) shows supercell model of GaN which contains 16 Ga atoms and 16 N atoms. The coordinate of V_{Ga} is (0.66667, 0.33333, 0.49926) and that of V_N is (0.33333, 0.66667, 0.4375) (as shown in Figures 1(b) and 1(c)). The calculation is based on the CASTEP (Serial Total Energy Package Cambridge) of Material Studio 7.0 in this paper. The interaction between

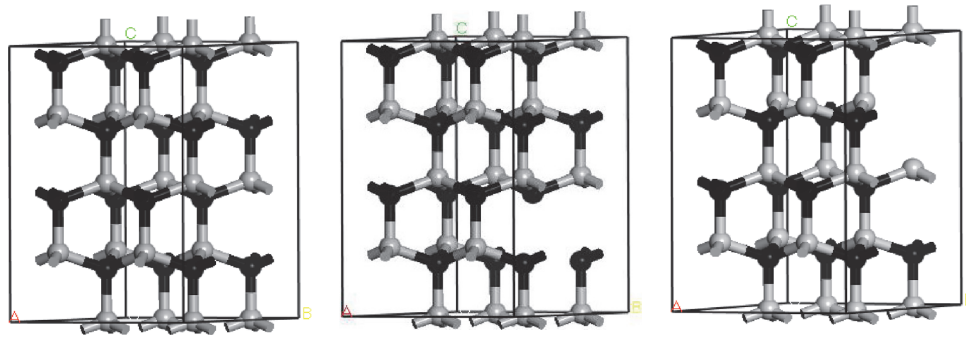

(a) (b) (c)

Figure 1: (a) 2 × 2 × 2 GaN supercell; black stands for N atoms and grey stands for Ga atoms, (b) GaN with Ga vacancy (GaN:V_{Ga}), and (c) GaN with N vacancy (GaN:V_N).

Table 1: Lattice parameters of GaN after geometry optimization.

	a/nm	c/nm	c/a
GaN (Exp)	0.3189	0.5185	1.626
GaN	0.3226	0.5253	1.628
GaN:V_N	0.3229	0.5241	1.623
GaN:V_{Ga}	0.3224	0.5263	1.632

electrons and ions is described by means of plane wave pseudopotential method (PWP) with generalized gradient approximation (GGA). Energy cut-off of plane wave is 360 eV. The convergent accuracy is 2×10^{-6} eV/atom during iteration. The maximum force is 0.03 eV/A and the maximum stress is 0.05 GPa. Monkhorst-Pack is used to calculate the total energy and charge density in the Brillouin zone. K-point set is 4 × 4 × 2. Fast Fourier transform (FFT) grid is 40 × 40 × 72. All the calculations are carried out in the reciprocal space. The valency electrons in calculation are Ga: $3d^{10}4s^24p^1$, N:$2s^22p^3$.

3. Results and Discussions

3.1. Structure and Properties. Table 1 shows the lattice constants of pure and vacancy defects GaN after optimization. c/a is 1.628 in pure GaN, which is close to others' [9]. The error is only 0.12% comparing with experimental results 1.626. The lattice constant c decreases in GaN:V_N and increases in GaN:V_{Ga}. However, vacancy type has a little effect on the lattice constant a. This result is similar to the literature [10]. The result indicates that V_N causes a larger relaxation in [1000] direction, but V_{Ga} has larger relaxation in [0001] direction.

3.2. Band Structure and Density of States. Figure 2 shows the band structure of the pure GaN and vacancy defects GaN. The valence band maximum and conduction band minimum of pure GaN are located in the G point of Brillouin zone. The results indicate that GaN is a direct wide band gap semiconductor material with energy gap of 1.66 eV. This result is consistent with Du et al.'s [11]. But it is significantly different from the experimental value of 3.39 eV. This is due to the use of the generalized gradient approximation (GGA) and ignoring the correlation of excited state electrons. It has no effect on result discussion [12]. It can be seen from Figure 2 that the numbers of valence band and conduction band significantly increase in GaN:V_{Ga} and GaN:V_N and the band gap is wider than that of the pure GaN. The band gaps of GaN:V_N and GaN:V_{Ga} increase to 2.30 eV and 1.97 eV, respectively. GaN becomes an indirect band gap semiconductor because of V_N. Three acceptor levels are introduced at 0.67 eV near the top of valence band in GaN:V_{Ga}. The Fermi level (E_f) moves to lower energy regions obviously. The Fermi level occupies the part of valence band maximum. Electrons in valence band can jump to this level. Holes can occur in the valence band. So Ga vacancy is acceptor defect in GaN.

The total density of states (TDOS) of pure GaN and vacancy defect GaN is shown in Figure 3. It can be seen from Figure 3 that the valence band of pure GaN is mainly composed of two group bands. The valence band above is mainly from Ga3d and N2s states. It ranges from −15.9 eV to −10.4 eV. The peak of Ga3d state appears at −13.5 eV and forms a strong local density of states. There are no obvious interactions with other valence bands. The valence band below is from −6.9 eV to 0 eV. It is mainly composed of N2p state which determines the position of valence band. The conduction band is from 3.0 eV to 7.7 eV. It mainly consists of Ga4s and Ga4P states and a few of N2p states. N2s states have less contribution to the valence and conduction band. Near the Fermi level, the variation of DOS at the bottom of the conduction band is relatively smooth. The electron has a small effective mass and high mobility in the conduction band [13]. Figure 3(b) shows that V_N has great effect on the TDOS of GaN. The valence and conduction band of GaN:V_N move to lower energy regions obviously. The conduction band minimum shifts to lower energy and occupies the Fermi level. A shallow donor level is produced at the bottom of the conduction band and its width is about 0.8 eV. GaN presents n-type conductivity. The valence band of GaN:V_{Ga} moves to higher energy regions and the Fermi level jumps into the valence band. But the movement is relatively small. The Fermi level occupies part of the valence band maximum. The electrons in the valence band jump to this level and holes are produced in the valence band. V_{Ga} is the acceptor

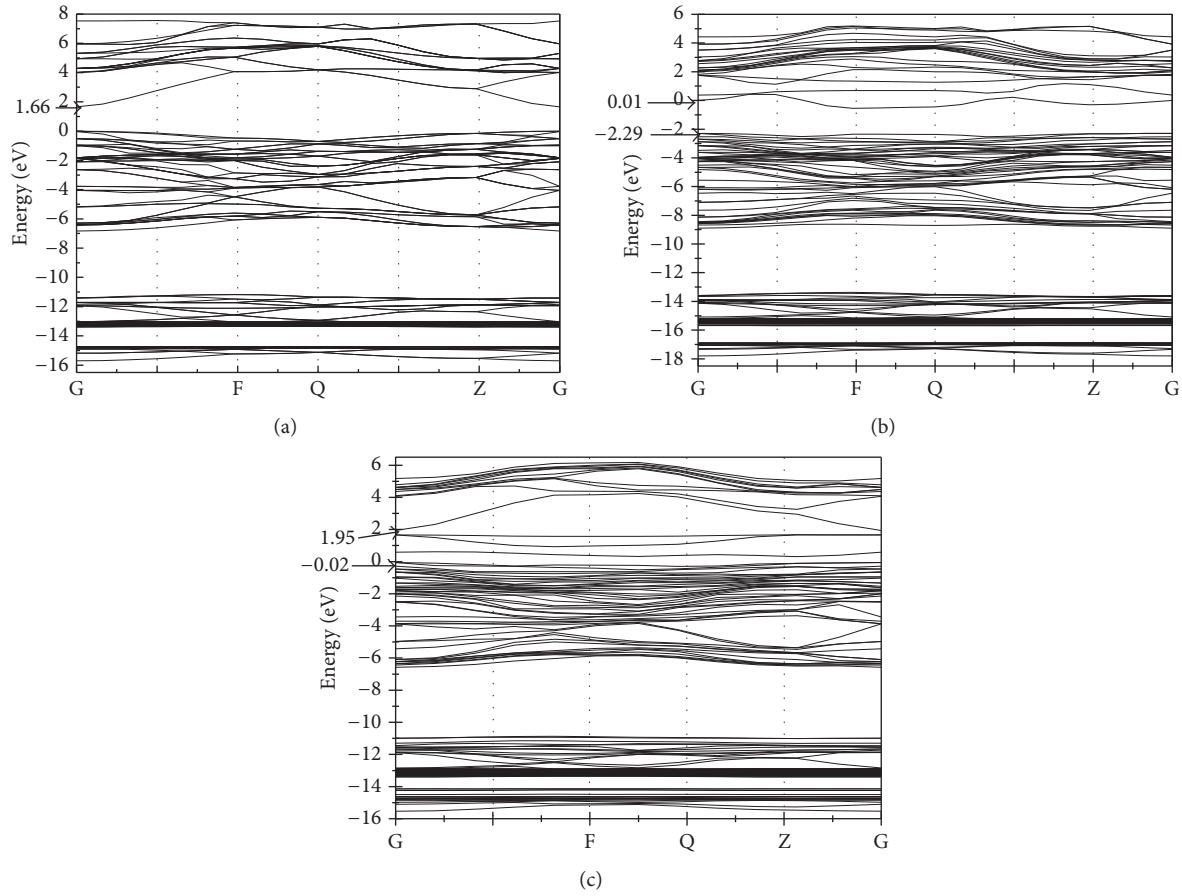

Figure 2: Band structure of pure GaN (a), GaN:V_N (b), and GaN:V_{Ga} (c).

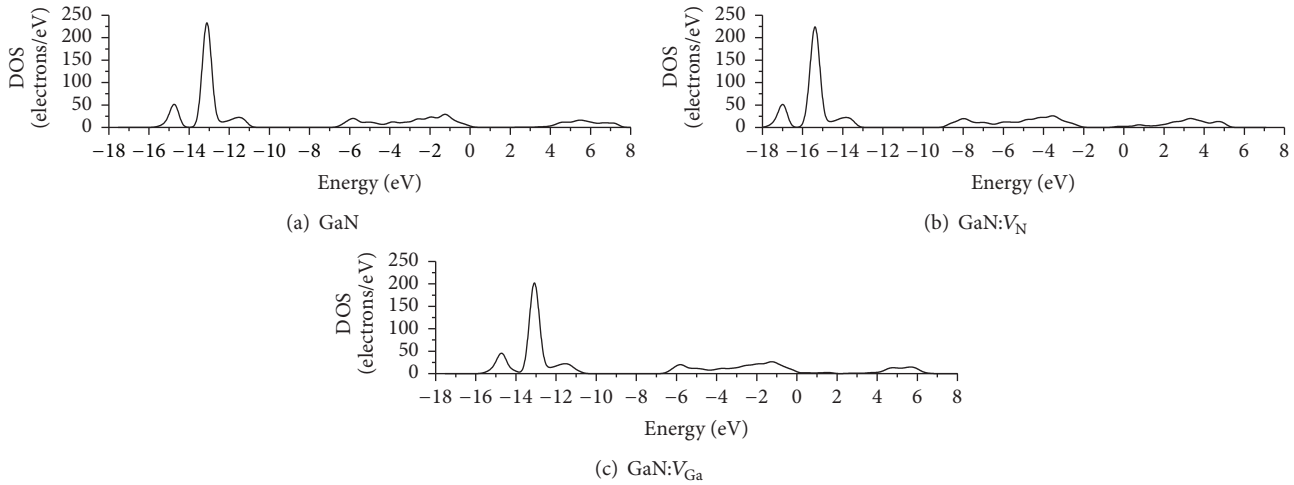

Figure 3: Total density of state of pure and vacancy GaN.

defect for GaN. The peak of DOS decreases significantly in the valence band of GaN:V_N and GaN:V_{Ga}. The peak of GaN:V_{Ga} decreases more obviously. The density of states in GaN:V_N shows a significant decline near the Fermi level. The conductivity is proportional to the density of states at the Fermi level. So we can confirm that V_N can reduce the conductivity of GaN. It is also found that vacancy causes band gap increase from Figure 3.

Figures 4 and 5 show the partial density of states of Ga and N atoms, respectively. The bottom of the conduction band is mainly determined by the Ga4s electron states in the pure and vacancy defects GaN. It can be seen from Figure 5(c) that

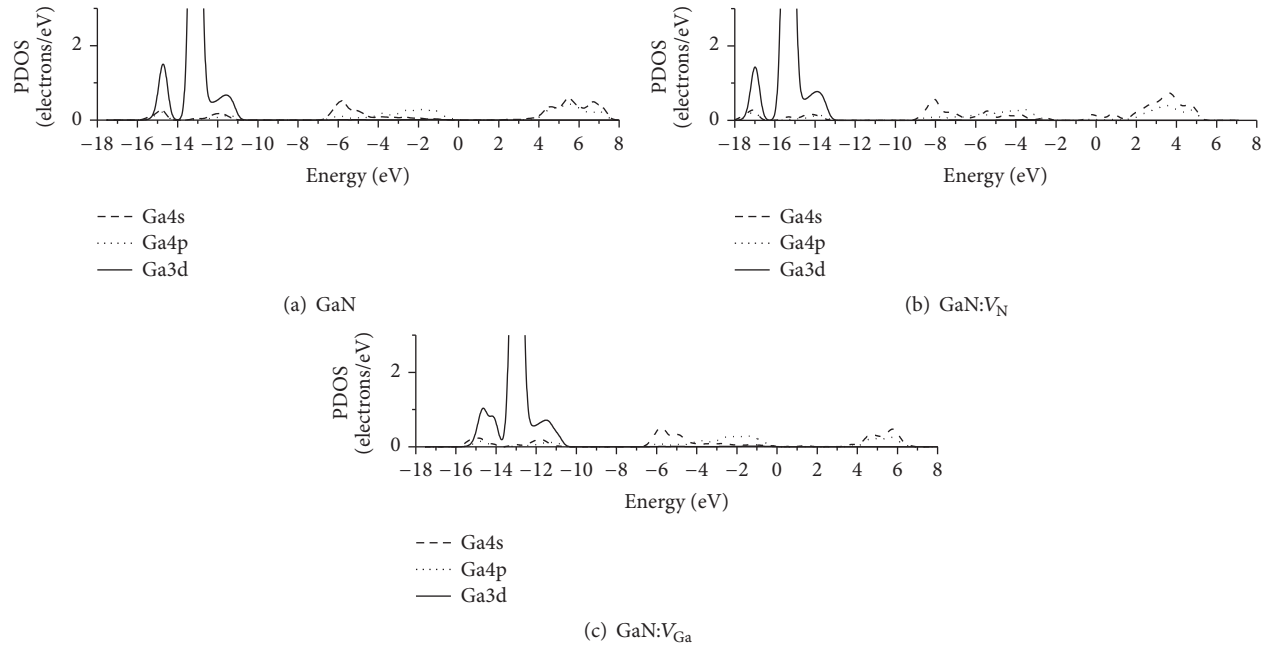

Figure 4: Partial density of state of Ga atom.

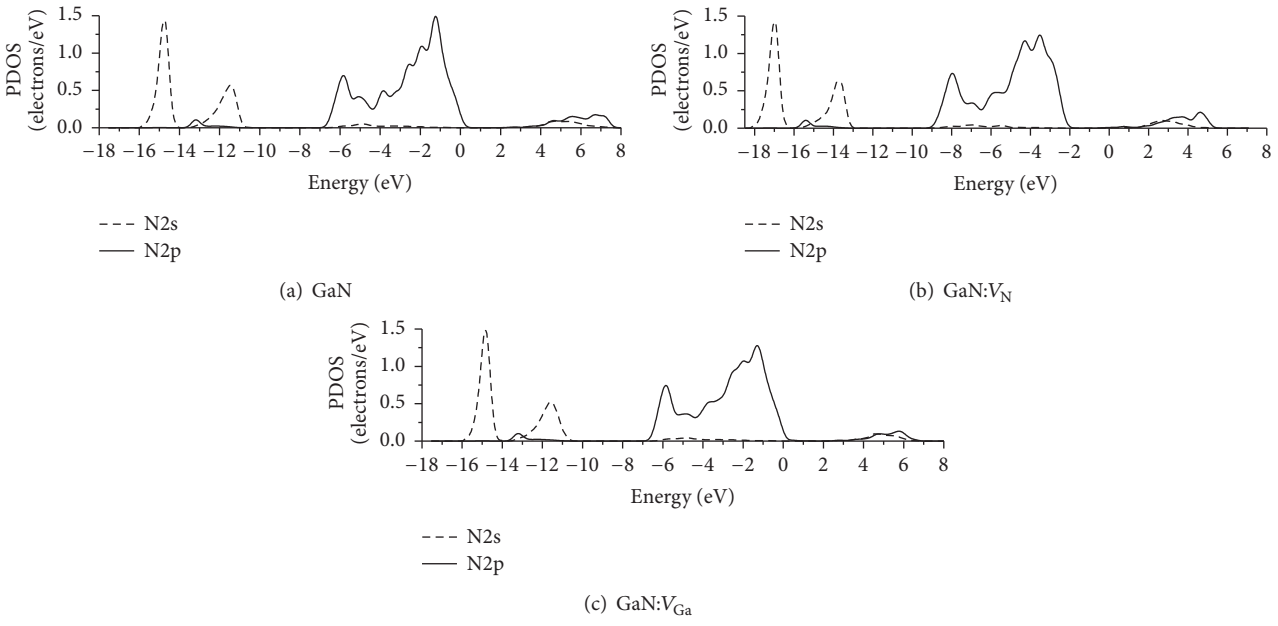

Figure 5: Partial density of state of N atom.

the acceptor level in the valence band maximum of GaN:V_{Ga} is mainly contributed by N2p electron states. N2p electrons cross Fermi level to occupy a higher energy level. Unfilled electron states are formed at the top of valence band. GaN presents p-type conductivity. Figure 5(b) shows that N2p states of GaN:V_N form level splitting at −4 eV and 4 eV. This may be the S-like and P-like local states caused by V_N [14]. S-like states are in the valence band and P-like states are in the conduction band. Instead of level splitting, a greater level is formed in GaN:V_{Ga} as shown in Figure 5(c). We can see from Figure 4(c) that Ga3d states of GaN:V_{Ga} form two split levels at about −15 eV. The two levels are 0.8 eV apart. It is believed that the main reason for the level splitting is the quantum effect interactions between atoms. The absence of Ga atoms destroys the periodic structure of the perfect GaN. N atoms superposition and hybridization with Ga cause Ga3d states split below valence band in GaN:V_{Ga}.

3.3. Influence of Defects on the Optical Properties of GaN. Adiabatic approximation and single electron approximation

are usually used in the interaction between light and solid. The phonon indirect transition can be neglected using the single electron approximation. Only electronic excitation is considered [15]. Complex permittivity is $\varepsilon(\omega) = \varepsilon_1(\omega) + i\varepsilon_2(\omega)$ and complex refractive index is $N(\omega) = n(\omega) + ik(\omega)$, which can describe the linear response of the system to the photoelectric field in the wavelet vector. The imaginary part of the dielectric constant can be deduced according to the direct transition probability and dispersion relationship [16]:

$$\varepsilon_2(\omega) = \frac{C}{\omega^2} \sum_{C,V} \int_{BZ} \frac{2}{(2\pi)^3} \left| M_{CV}(K) \right|^2 \times \delta\left(E_{kC} - E_{kV} - h\omega\right) d^3K. \quad (1)$$

The subscripts of C and V are the conduction band and valence band, respectively. BZ is the first Brillouin zone. K is the electron wave vector. $M_{CV}(K)$ is the transition matrix element. E_{KC} and E_{KV} are the intrinsic levels of the conduction band and valence band. Formula (1) provides the basic theoretical basis for the analysis of the structure and optical properties of crystal. It reflects the luminescence mechanism of the electronic transitions between levels. The spectra are generated by electronic transitions between levels. Each dielectric peak can be explained by band structure and density of states [17].

The imaginary dielectric functions of the pure GaN and vacancy defect GaN are given in Figure 6. It can be seen from Figure 6 that a very strong peak appears in the range of 5–10 eV. The principal peak of pure GaN is located at 5.89 eV. It is supposed to be caused by the Ga3d or N2p electrons transition to lower levels. The principal peak in GaN:V_N and GaN:V_{Ga} shifts to higher energy regions slightly. The spectrum shows blueshift. The intensity of the principal peak is weakened. This is due to the lattice relaxation induced by vacancy in GaN. There is no dielectric peak in 0–2 eV in pure GaN. But dielectric peak is found at about 0.82 eV in GaN:V_N and GaN:V_{Ga}. And the peak in GaN:V_N is stronger. This peak comes from the transition between valence band and conduction band. The peak at 2.83 eV in the pure GaN should be N2p electrons transition from valence band maximum to conduction band. There is deviation between the peak and energy gap, which is probably related to the relaxation effect of N2p electrons transition. The peak becomes a rising edge and shifts to higher energy regions in GaN:V_N. It is consistent with the band gap increase in GaN:V_N. Ga vacancy will introduce a deep acceptor level near the Fermi level. So the peak at 2.83 eV in GaN:V_{Ga} is considered to be the transition between the conduction band and the deep acceptor level. Ga vacancy was once believed to be the source of yellow light (2.2–2.8 eV) [18]. The peaks are the same at 10.97 eV and 18.22 eV in pure and vacancy GaN. The peak at 10.97 eV may be the Ga3d or N2s electrons transition between the valence band above and below. The peak at 18.22 eV should be the Ga3d transition between the valence band below and the conduction band. Most electrons in valence band below jump to valence band above in the first and then transit from valence band above to conduction band. There are few electrons transitioning from valence band below to conduction band directly. So the peak is very weak.

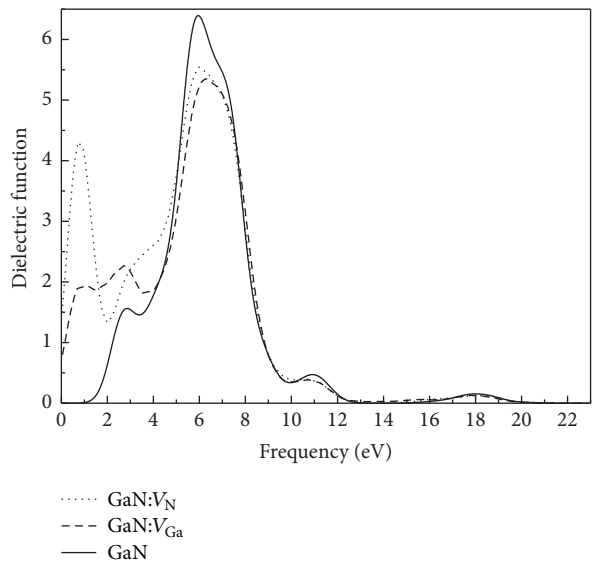

Figure 6: The imaginary part of the complex dielectric function of the pure and vacancy defects GaN.

4. Conclusions

The electronic structure and optical properties of pure GaN and GaN:V_N, GaN:V_{Ga} have been investigated by means of plane wave pseudopotential method (PWP) with generalized gradient approximation (GGA). The vacancy defects make lattice constant change and band gap increase. The valence and conduction band shift to lower energy regions obviously in GaN:V_N compared with pure GaN. The valence band moves to higher energy regions in GaN:V_{Ga}. Vacancy makes the density of state decrease obviously in the valence band below of GaN. The peak decreases more in the GaN:V_{Ga}. Ga4s electron states decide the conduction band minimum and the valence band maximum is determined by N2p states in pure GaN, GaN:V_N, and GaN:V_{Ga}. Optical properties are induced by vacancy defects. New dielectric peaks appear in lower energy regions in GaN:V_N and GaN:V_{Ga}. The peaks are produced by electronic transitions from the valence band to the conduction band. Compared with pure GaN, the principal peaks in GaN:V_N and GaN:V_{Ga} shift to higher energy region slightly. At the same time, the intensity is weakened and blueshift happened.

Competing Interests

The authors declare that they have no competing interests.

Acknowledgments

This work was supported by the Langfang City Key Technology Research and Development Program of China (no.

2016011054) and the Fundamental Research Funds for the Central Universities of China (no. 3142016010).

References

[1] A. Majid, J. Iqbal, and A. Ali, "Structural, optical and magnetic properties of Ce-GaN based diluted magnetic semiconductor," *Journal of Superconductivity and Novel Magnetism*, vol. 24, no. 1-2, pp. 585–590, 2011.

[2] Q. Q. Li, Q. Y. Hao, Y. Li, and G. Liu, "First principle study of Ce doping and related complexes in GaN," *Computational Materials Science*, vol. 72, pp. 32–37, 2013.

[3] J. K. Shen and F. W. Huang, "Improved conversion efficiency of GaN-based solar cells with Mn-doped absorption layer," *Applied Physics Letters*, vol. 103, no. 6, Article ID 063906, 4 pages, 2013.

[4] A. Majid, A. Dar, and J. J. Zhu, "Cerium induced ferromagnetic exchange interactions in GaN," *Journal of Magnetism and Magnetic Materials*, vol. 374, pp. 676–679, 2015.

[5] J. Neugebauer and C. G. Van De Walle, "Atomic geometry and electronic structure of native defects in GaN," *Physical Review B*, vol. 50, no. 11, pp. 8067–8070, 1994.

[6] P. Boguslawski, E. L. Briggs, and J. Bernholc, "Native defects in gallium nitride," *Physical Review B*, vol. 51, no. 23, pp. 17255–17258, 1995.

[7] J. Kang, D. Cai, X. Xiao, Y. Shen, and B. Shen, "Defects in III nitrides epilayers," *Research and Progress of Solid State Electronics*, vol. 22, no. 4, pp. 375–380, 2002.

[8] Y.-W. Shen and J.-Y. Kang, "Ab initio calculation of the electronic structure of carbon and oxygen impurities in GaN," *Wuli Xuebao/Acta Physica Sinica*, vol. 51, no. 3, pp. 645–648, 2002.

[9] G. Y. Gao, K. L. Yao, Z. L. Liu, Y. L. Li, Y. C. Li, and Q. M. Liu, "Ab initio pseudopotential studies of the pressure dependences of structural, electronic and optical properties for GaN," *Solid State Communications*, vol. 138, no. 10-11, pp. 494–497, 2006.

[10] W. E. Packard, J. D. Dow, K. Doverspike, R. Kaplan, and R. Nicolaides, "Vacancy structures on the GaN(0001) surface," *Journal of Materials Research*, vol. 12, no. 3, pp. 646–650, 1997.

[11] Y.-J. Du, B.-K. Chang, J.-J. Zhang, B. Li, and X.-H. Wang, "First-principles study of the electronic structure and optical properties of GaN(0001) surface," *Acta Physica Sinica*, vol. 61, no. 6, pp. 414–420, 2012.

[12] S. Zhang, J. Shi, M. Zhang, M. Yang, and J. Li, "First-principles investigation on optical properties of GaN and InGaN alloys," *Journal of Physics D: Applied Physics*, vol. 44, no. 49, pp. 495304–495312, 2011.

[13] Z. Dridi, A. Lazreg, H. Rozale et al., "Electronic structure and magnetism of cubic $Ga_{1-x}Eu_xN$ and $Al_{1-x}Eu_xN$ using the LSDA+U approach," *Computational Materials Science*, vol. 48, no. 4, pp. 743–748, 2010.

[14] E. Yamaguchi and M. R. Junnarkar, "Effects of nitrogen vacancy on optical properties of nitride semiconductors," *Journal of Crystal Growth*, vol. 189-190, pp. 570–574, 1998.

[15] R. P. Davies, C. R. Abernathy, S. J. Pearton, D. P. Norton, M. P. Ivill, and F. Ren, "Review of recent advances in transition and lanthanide metal-doped GaN and ZnO," *Chemical Engineering Communications*, vol. 196, no. 9, pp. 1030–1053, 2009.

[16] X. C. Sheng, *The Spectrum and Optical Property of Semiconductor*, Science Press, Beijing, China, 2003.

[17] K. Huang and R. Q. Han, *Solid State Physics*, Higher Education Press, Beijing, China, 1988.

[18] A. Sedhain, J. Li, J. Y. Lin, and H. X. Jiang, "Nature of deep center emissions in GaN," *Applied Physics Letters*, vol. 96, no. 15, pp. 1902–1907, 2010.

Hindawi
Journal of Nanotechnology
Volume 2017, Article ID 4030249, 7 pages
https://doi.org/10.1155/2017/4030249

Research Article

Synthesis of xLiMnPO$_4$·yLi$_3$V$_2$(PO$_4$)$_3$/C Nanocomposites for Lithium Ion Batteries Using Tributyl Phosphate as Phosphor Source

Yanming Wang, Bo Zhu, Xiaoyu Liu, and Fei Wang

Anhui Key Laboratory of Energetic Materials and School of Chemistry and Materials Science, Huaibei Normal University, Huaibei, Anhui 235000, China

Correspondence should be addressed to Fei Wang; wangfeichem@126.com

Received 13 November 2016; Accepted 25 December 2016; Published 15 January 2017

Academic Editor: Xuanhua Li

Copyright © 2017 Yanming Wang et al. This is an open access article distributed under the Creative Commons Attribution License, which permits unrestricted use, distribution, and reproduction in any medium, provided the original work is properly cited.

The xLiMnPO$_4$·yLi$_3$V$_2$(PO$_4$)$_3$/C (x/y = 1 : 0, 12 : 1, 8 : 1, 6 : 1, 4 : 1, 0 : 1) composite cathode materials are synthesized using tributyl phosphate as a novel organic phosphor source via a solid-state reaction process. All obtained xLiMnPO$_4$·yLi$_3$V$_2$(PO$_4$)$_3$/C composites present similar particles morphology with an average size of ca. 100 nm and low extent agglomeration. The electrochemical performance of pristine LiMnPO$_4$/C can be effectively improved by adding small amounts of Li$_3$V$_2$(PO$_4$)$_3$ additives. The 4LiMnPO$_4$·Li$_3$V$_2$(PO$_4$)$_3$/C has a high discharge capacity of 143 mAh g^{-1} at 0.1 C and keeps its 94% at the end of 100 cycles.

1. Introduction

Recently, 4 V olivine-structured LiMnPO$_4$ and monoclinic Li$_3$V$_2$(PO$_4$)$_3$ attract much attention as polyanionic cathode materials for lithium ion batteries because of their superior thermal and cycling stabilities [1–4]. LiMnPO$_4$, owing to the outstanding advantages of low cost and nontoxicity, exhibits more attraction than Li$_3$V$_2$(PO$_4$)$_3$ for use in power batteries and energy storage systems. However, the one-dimensional Li$^+$ transport pathway in LiMnPO$_4$ crystal restricts its electrochemical performance at high charge-discharge currents [5]. By contrast, the open three-dimensional pathway in Li$_3$V$_2$(PO$_4$)$_3$ crystal enables fast Li$^+$ migration, resulting in the high rate capability [6]. However, the relatively high cost of raw materials for Li$_3$V$_2$(PO$_4$)$_3$ hinders its large amount of industrial production.

More recently, several reports have proved that the electrochemical activity of bulk LiMnPO$_4$ can be effectively enhanced by incorporating with a small amount of Li$_3$V$_2$(PO$_4$)$_3$ additives [7–9]. On one hand, the structure modification of V doping at Mn sites can increase the electronic and ionic transport speed of LiMnPO$_4$ phase [10–12]. On the other hand, the homogeneous dispersion of Li$_3$V$_2$(PO$_4$)$_3$ crystallites in LiMnPO$_4$ body reduces Li-diffusion distance in the LiMnPO$_4$[13]. Li et al. [14] prepared $(1-x)$LiMnPO$_4$·xLi$_3$V$_2$(PO$_4$)$_3$/C composites through a sol-gel route, and 0.5LiMnPO$_4$·0.5Li$_3$V$_2$(PO$_4$)$_3$/C showed the highest discharge capacity of 135 mAh g^{-1} at 0.1 C. Zhang et al. [15] synthesized LiMnPO$_4$·Li$_3$V$_2$(PO$_4$)$_3$/C using rod-like MnV$_2$O$_6$·4H$_2$O as precursor, which provided a reversible capacity of 126 mAh g^{-1} at 0.1 C. Chen et al. [16] reported the synthesis of 0.95LiMn$_{0.95}$Fe$_{0.05}$PO$_4$·Li$_3$V$_2$(PO$_4$)$_3$ composite, which exhibited capacity of 176 mAh g^{-1} at 0.05 C and retained 112 mAh g^{-1} after 50 cycles. Qin et al. [17] synthesized the LiMnPO$_4$-Li$_3$V$_2$(PO$_4$)$_3$/C composite materials at the sintering temperature of 600°C. The 0.6LiMnPO$_4$·0.4Li$_3$V$_2$(PO$_4$)$_3$ exhibits the highest discharge capacity of 126 mAh g^{-1} at 0.1 C, against 76 mAh g^{-1} for the pristine LiMnPO$_4$/C. Similarly, the synergistic effect of LiFePO$_4$ and Li$_3$V$_2$(PO$_4$)$_3$ on physical and electrochemical behaviors is extensively investigated in recent studies [18–24].

It is noteworthy that the particle size, carbon layer, and phase distribution strongly affect the electrochemical activity of LiMnPO$_4$-Li$_3$V$_2$(PO$_4$)$_3$ composite. In this paper, we use

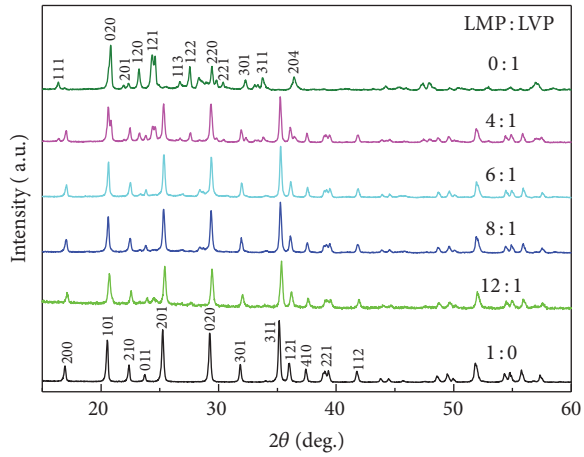

Figure 1: XRD patterns of the xLMP·yLVP/C samples.

tributyl phosphate as a novel organic phosphor source to synthesize a series of $x\text{LiMnPO}_4 \cdot y\text{Li}_3\text{V}_2(\text{PO}_4)_3$/C (abbreviated as xLMP·yLVP/C) composites by ball-milling followed by sintering process. The physical and electrochemical properties of LiMnPO_4-based composites with different $\text{Li}_3\text{V}_2(\text{PO}_4)_3$ amounts are studied in detail.

2. Experimental

Stoichiometric Li_2CO_3, $\text{Mn(CH}_3\text{COO)}_2 \cdot 4\text{H}_2\text{O}$, V_2O_5, $(\text{C}_4\text{H}_9\text{O})_3\text{PO}$, and glycine were used as raw materials. Glycine acted as carbon source and the carbon amount of final products was controlled about 5 wt%. Appropriate quantities of reactants were ball-milled in ethanol for 6 h at 350 rpm. The obtained mixture was dried at 70°C and then heated at 700°C under Ar atmosphere for 10 h to yield the xLMP·yLVP/C (x/y = 1 : 0, 12 : 1, 8 : 1, 6 : 1, 4 : 1, 0 : 1) cathode materials.

X-ray diffraction study was performed on X'pert Pro diffractometer equipped with Cu Kα radiation at 30 mA and 40 kV. Field-emission scanning electron microscope (FE-SEM, HITACHI-S4800) and high-resolution transmission electron microscope (HRTEM, JEOL-2100F) were used to investigate the morphology, crystal structure, and elemental distribution of the samples. The residual carbon amount was evaluated by PE 2400 elemental analyzer.

The electrochemical properties were studied by charge-discharge cycling using CR2016 coin-type cells. The cathode materials comprised xLMP·yLVP/C, acetylene black, and poly(vinylidene fluoride) with a weight ratio of 8 : 1 : 1. Lithium-foil is used as anode, Entek ET20-26 microporous membrane as separator, and 1 M LiPF_6 in ethylene carbonate/dimethyl carbonate (1 : 1, volume) as electrolyte. The assembled cells were cycled on a LANHE CT2001 battery testing system with a constant current-constant voltage mode between 2.0 and 4.5 V at 25°C. Cyclic voltammetry (CV) was conducted on a Chenhua CHI650D electrochemical workstation at a sweep rate of 0.1 mV s^{-1}.

3. Results and Discussion

Figure 1 shows the XRD patterns of the as-prepared composites. The diffraction peaks in the sample with x/y = 1 : 0 can be assigned to olivine LiMnPO_4 (space group *Pnmb*, JCPDS 74-0375) [1]. As x/y = 0 : 1, all peaks can be indexed to monoclinic $\text{Li}_3\text{V}_2(\text{PO}_4)_3$ (space group $P2_1/n$, JCPDS 47-0107) [22]. When x/y = 12 : 1, 8 : 1, 6 : 1, and 4 : 1, the diffraction peaks of xLMP·yLVP/C consist of LiMnPO_4 and $\text{Li}_3\text{V}_2(\text{PO}_4)_3$ phases without any crystalline impurity. The diffraction peaks of $\text{Li}_3\text{V}_2(\text{PO}_4)_3$ become stronger with increasing $\text{Li}_3\text{V}_2(\text{PO}_4)_3$ amount. No detectable reflections for graphitic carbon are observed, which suggests that carbon in all composites is amorphous.

Figure 2 compares the powder morphologies of LMP/C, 8LMP·LVP/C, 4LMP·LVP/C, and LVP/C samples. All samples exhibit narrow particle size distribution with an average size of ca. 100 nm. Tributyl phosphate is a liquid organic molecule, compared with solid $\text{NH}_4\text{H}_2\text{PO}_4$, which can favorably disperse in the precursors during ball-milling process. The decomposition of tributyl phosphate releases gas and forms some in situ carbon layer on the surface of xLMP·yLVP nuclei during the heating step. This effectively prevents the aggregation of small primary particles and further growth.

TEM image of 4LMP·LVP/C in Figure 3(a) displays that the primary 4LMP·LVP nanoparticles are connected by amorphous carbon. The corresponding elemental mappings for Mn, V, and P illustrate that the LiMnPO_4 particle contains $\text{Li}_3\text{V}_2(\text{PO}_4)_3$ phase and the $\text{Li}_3\text{V}_2(\text{PO}_4)_3$ particle contains LiMnPO_4 phase (Figures 3(b)–3(d)). The atomic ratio of Mn/V/P presented in EDS spectrum basically accords with the theoretical value of 4LMP·LVP/C (Figure 3(e)). HRTEM image of 4LMP·LVP/C in Figure 3(f) shows that the particle surface is fully coated with amorphous carbon layer. The d-spacing values of 0.524 and 0.352 nm correspond to the (020) and (111) crystalline planes of LiMnPO_4, respectively, whereas the d-spacing value of 0.431 nm is attributed to the (020) plane of $\text{Li}_3\text{V}_2(\text{PO}_4)_3$. The results demonstrate that both LiMnPO_4

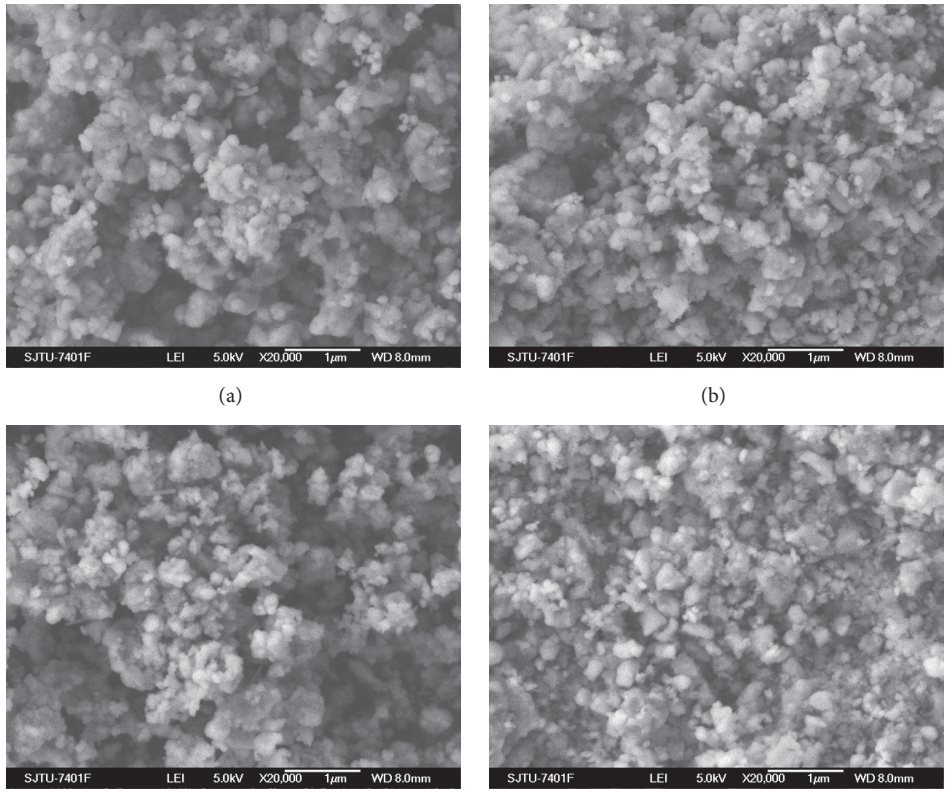

Figure 2: SEM images of LMP/C (a), 8LMP·LVP/C (b), 4LMP·LVP/C (c), and LVP/C (d) samples.

and $Li_3V_2(PO_4)_3$ nanocrystals coexist in the 4LMP·LVP/C particles.

Figure 4 displays the typical charge-discharge and cycle life profiles of the *x*LMP·*y*LVP/C samples at 0.1 C. As shown in Figure 4(a), the LMP/C gives one reversible voltage plateau nearby 4.1 V associating with the phase transition of $LiMnPO_4 \leftrightarrow MnPO_4$, while the LVP/C presents three reversible voltage plateaus nearby 3.6 V, 3.7 V, and 4.1 V corresponding to the sequential phase transitions of $Li_3V_2(PO_4)_3 \leftrightarrow Li_{2.5}V_2(PO_4)_3 \leftrightarrow Li_2V_2(PO_4)_3 \leftrightarrow LiV_2(PO_4)_3$, respectively [9]. As to the *x*LMP·*y*LVP/C composites, the distinct voltage plateaus of both $LiMnPO_4$ and $Li_3V_2(PO_4)_3$ are observed. Furthermore, the electrochemical polarization of $LiMnPO_4$ is effectively alleviated by $Li_3V_2(PO_4)_3$ additive, especially in the 4LMP·LVP/C composite. The discharge capacities of *x*LMP·*y*LVP/C composites with various *x*/*y* of 12 : 1, 8 : 1, 6 : 1, and 4 : 1 are 115, 124, 131, and 143 mAh g^{-1}, respectively, much higher than that of LMP/C (102 mAh g^{-1}). Figure 4(b) describes the cycle life profiles of the composite samples. After 100 cycles at 0.1 C, the capacity retention for LMP/C, 12LMP·LVP/C, 8LMP·LVP/C, 6LMP·LVP/C, and 4LMP·LVP/C is 98%, 96%, 95%, 95%, and 94%, demonstrating good cycling stability. By contrast, the LVP/C provides relatively lower capacity retention of 90% than the LMP-based composites, in spite of delivering the largest initial discharge capacity of 155 mAh g^{-1}. Here, the capacity fade of *x*LMP·*y*LVP/C can be ascribed to the irreversible structural changes of $Li_3V_2(PO_4)_3$ when cycling a part of the third Li^+ beyond 4.3 V [17].

Figure 5 exhibits the discharge rate profiles of LMP/C and 4LMP·LVP/C samples ranging from 0.1 C to 2 C. Obviously, the discharge capacities of 4LMP·LVP/C remarkably surpass that of LMP/C at various rates. Moreover, the 4LMP·LVP/C can retain much higher discharge voltage plateau than LMP/C at high rates, such as at 1 C and 2 C. According to the HRTEM and EDS analysis in Figure 3, the $LiMnPO_4$ primary particle is further divided by a small amount of $Li_3V_2(PO_4)_3$ nanocrystals, which shortens Li-diffusion distance in $LiMnPO_4$ body resulting in the superior rate capability.

Figure 6 shows the typical cyclic voltammetry profiles of the *x*LMP·*y*LVP/C electrodes between 3.0 and 4.5 V. One redox couple peak at 3.92/4.33 V for LMP/C belongs to the reaction of $Mn^{2+} \leftrightarrow Mn^{3+}$. Meanwhile, three redox couple peaks at 3.56/3.61, 3.64/3.69, and 4.02/4.11 V for LVP/C correspond to the reaction of $V^{3+} \leftrightarrow V^{4+}$. For the 12LMP·LVP/C, 8LMP·LVP/C, 6LMP·LVP/C, and 4LMP·LVP/C samples, the redox couple peaks of $LiMnPO_4$ and $Li_3V_2(PO_4)_3$ are both detected. More importantly, the interval between the Mn^{2+}/Mn^{3+} redox potential peaks decreases from 0.41 V of LMP/C to 0.33 V of all LMP-LVP/C composites. The CV results coincide with the charge-discharge profiles, which reveals that the electrochemical activity and reversibility of $LiMnPO_4$ are improved by incorporating with $Li_3V_2(PO_4)_3$.

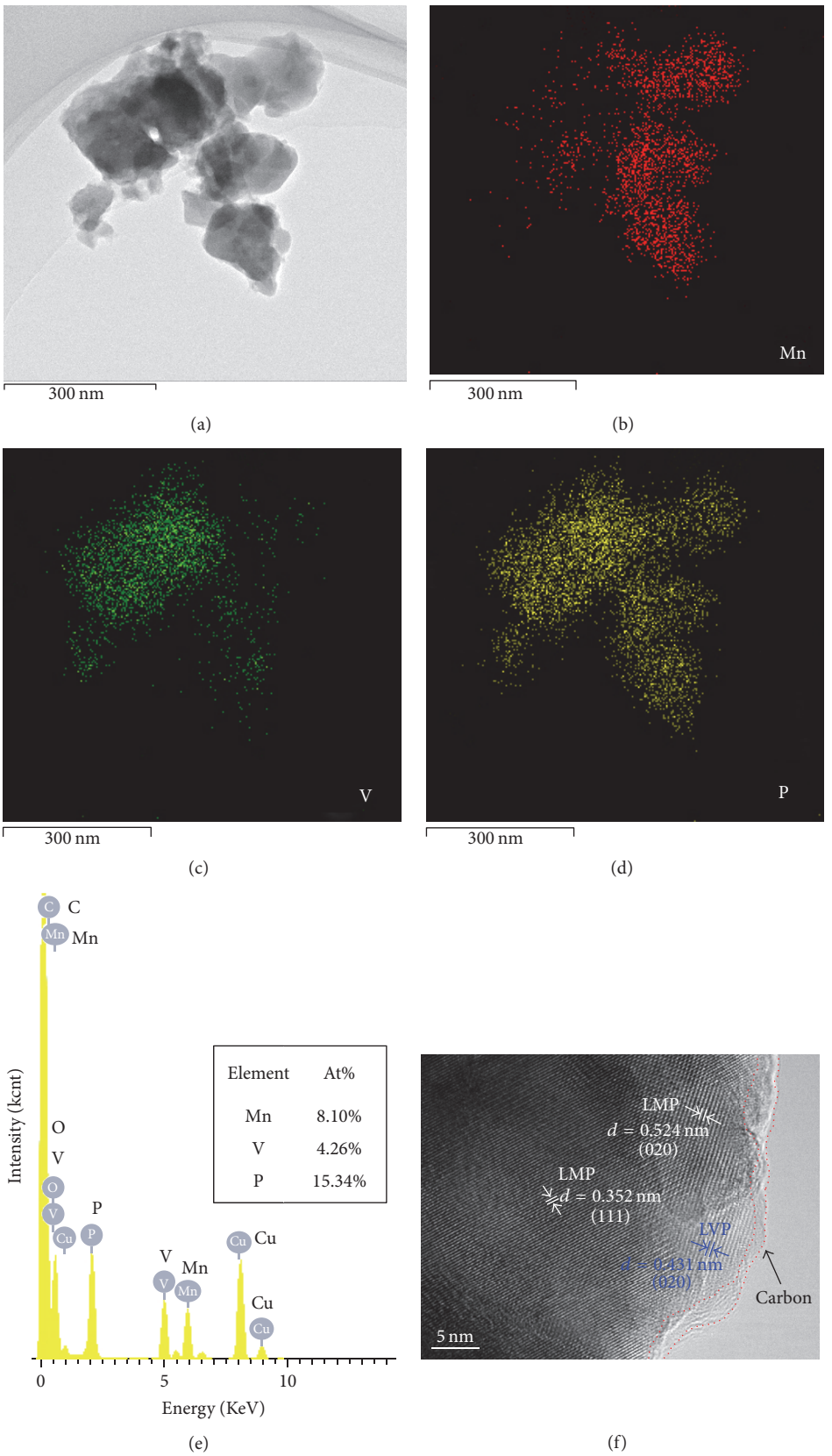

Figure 3: Elemental mappings for Mn, V, P ((a)–(d)); EDS spectrum (e); HRTEM image of 4LMP·LVP/C (f).

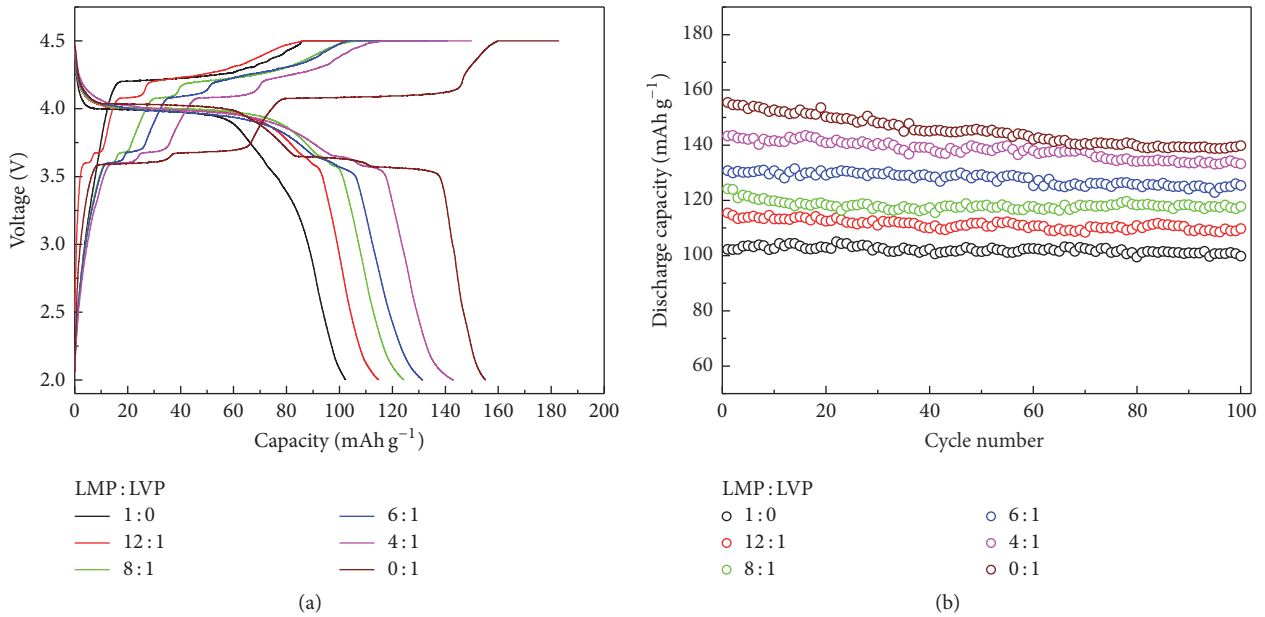

Figure 4: The charge-discharge capacity profiles (a) and cycle life profiles (b) of xLMP·yLVP/C at 0.1 C.

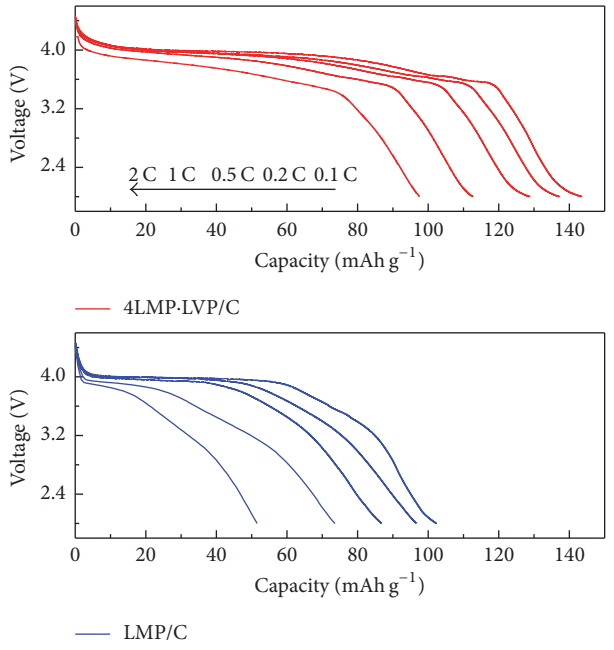

Figure 5: Discharge profiles of LMP/C and 4LMP·LVP/C at different C-rates.

4. Conclusions

In summary, the xLMP·yLVP/C nanoparticles are synthesized via a facile solid-state method using tributyl phosphate as phosphor source and glycine as carbon source. The use of tributyl phosphate is favorable for the formation of granular morphology with small particle size. XRD, HRTEM, and EDS mapping results indicate that the composites consist of $LiMnPO_4$ and $Li_3V_2(PO_4)_3$ phases, and the $Li_3V_2(PO_4)_3$ nanocrystals disperse in the $LiMnPO_4$ body particle. Among the LMP-LVP/C composites, the 4LMP·LVP/C delivers the largest discharge capacity of 143 mAh g^{-1} at 0.1 C along with superior rate capability and satisfactory cycle life. The LMP-LVP/C composite is promising as high-performance cathode material for rechargeable lithium batteries.

Competing Interests

The authors declare that they have no competing interests.

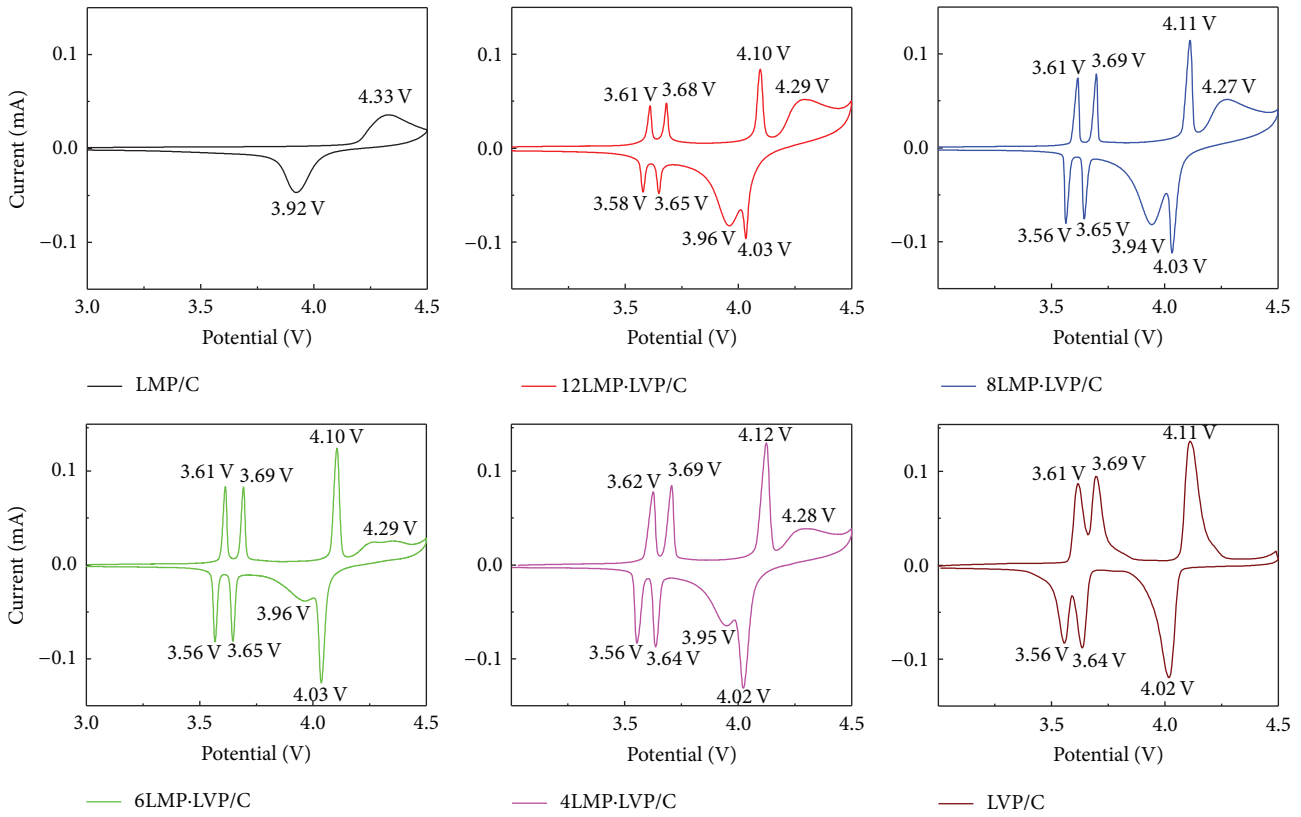

Figure 6: Cyclic voltammetry profiles of the xLMP·yLVP/C electrodes.

Acknowledgments

This study was supported by the National Natural Science Foundation of China (no. 21401061), Natural Science Foundation of Anhui Province, China (no. 1308085QB41), Provincial Natural Science Research Foundation of Anhui Universities, China (nos. KJ2014A224 and KJ2015A332), and the Key Project of Anhui Universities Support Program for Outstanding Youth, China (no. gxyqZD2016111).

References

[1] C. L. Hu, H. H. Yi, F. X. Wang et al., "Boron doping at P-site to improve electrochemical performance of $LiMnPO_4$ as cathode for lithium ion battery," *Journal of Power Sources*, vol. 255, pp. 355–359, 2014.

[2] T. Liu, Q. Xia, W. Lu, J. Xu, and X. Wu, "A novel method of preparing $LiMPO_4$-C nano particles with organic P source," *Electrochimica Acta*, vol. 174, no. 1, pp. 120–126, 2015.

[3] L. Wang, H. Liu, Z. Tang, L. Ma, and X. Zhang, "$Li_3V_2(PO_4)_3$/C cathode material prepared via a sol–gel method based on composite chelating reagents," *Journal of Power Sources*, vol. 204, pp. 197–199, 2012.

[4] K. Cui and Y. Li, "Monoclinic $Li_3V_2(PO_4)_3$/C nanocrystals co-modified with graphene nanosheets and carbon nanotubes as a three-dimensional-network cathode material for rechargeable lithium-ion batteries," *RSC Advances*, vol. 6, no. 10, pp. 8431–8439, 2016.

[5] Y. Hong, Z. Tang, W. Quan, S. Wang, and Z. Zhang, "Controllable synthesis of $LiMnPO_4$ nanocrystals: morphology evolution and their size-dependent electrochemical properties," *Ceramics International*, vol. 42, no. 4, pp. 8769–8778, 2016.

[6] M. Secchiaroli, F. Nobili, R. Tossici, G. Giuli, and R. Marassi, "Synthesis and electrochemical characterization of high rate capability $Li_3V_2(PO_4)_3$/C prepared by using poly(acrylic acid) and D-(+)-glucose as carbon sources," *Journal of Power Sources*, vol. 275, pp. 792–798, 2015.

[7] L. Wu, J. Lu, G. Wei et al., "Synthesis and electrochemical properties of $x LiMn_{0.9}Fe_{0.1}PO_4 \cdot y Li_3V_2(PO_4)_3$/C composite cathode materials for lithium-ion batteries," *Electrochimica Acta*, vol. 146, pp. 288–294, 2014.

[8] C. Wang, Y. Bi, Y. Liu, Y. Qin, Y. Fang, and D. Wang, "Investigation of $(1-x)LiMnPO_4 \bullet x Li_3V_2(PO_4)_3$/C: Phase composition and electrochemical performance," *Journal of Power Sources*, vol. 263, pp. 332–337, 2014.

[9] J.-F. Zhang, X.-W. Wang, B. Zhang, C.-L. Peng, H. Tong, and Z.-H. Yang, "Multicore-shell carbon-coated lithium manganese phosphate and lithium vanadium phosphate composite material with high capacity and cycling performance for lithium-ion battery," *Electrochimica Acta*, vol. 169, pp. 462–469, 2015.

[10] E. Dai, H. Fang, B. Yang, W. Ma, and Y. Dai, "Synthesis of vanadium doped $LiMnPO_4$ by an improved solid-state method," *Ceramics International*, vol. 41, no. 6, pp. 8171–8176, 2015.

[11] G. Yang, H. Ni, H. Liu et al., "The doping effect on the crystal structure and electrochemical properties of $LiMn_xM_{1-x}PO_4$ (M = Mg, V, Fe, Co, Gd)," *Journal of Power Sources*, vol. 196, no. 10, pp. 4747–4755, 2011.

[12] A. Gutierrez, R. Qiao, L. Wang, W. Yang, F. Wang, and A. Manthiram, "High-capacity, aliovalently doped olivine $LiMn_{1-3x/2}V_x\square_{x/2}PO_4$ cathodes without carbon coating," *Chemistry of Materials*, vol. 26, no. 9, pp. 3018–3026, 2014.

[13] F. Wang, J. Yang, Y. Nuli, and J. Wang, "Composites of $LiMnPO_4$ with $Li_3V_2(PO_4)_3$ for cathode in lithium-ion battery," *Electrochimica Acta*, vol. 103, pp. 96–102, 2013.

[14] S. Li, Z. Su, and X. Wang, "High performance $(1 - x)LiMnPO_4{\cdot}xLi_3V_2(PO_4)_3$/C composite cathode materials prepared by a sol-gel method," *RSC Advances*, vol. 5, no. 98, pp. 80170–80175, 2015.

[15] B. Zhang, X.-W. Wang, and J.-F. Zhang, "Novel synthesis of $LiMnPO_4{\bullet}Li_3V_2(PO_4)_3$/C composite cathode material," *RSC Advances*, vol. 4, no. 90, pp. 49123–49127, 2014.

[16] L. Chen, B. Yan, H. Wang, X. Jiang, and G. Yang, "Synthesis and characterization of $0.95LiMn_{0.95}Fe_{0.05}PO_4{\cdot}0.05Li_3V_2(PO_4)_3$ nanocomposite by sol–gel method," *Journal of Power Sources*, vol. 287, pp. 316–322, 2015.

[17] L. Qin, Y. Xia, B. Qiu, H. Cao, Y. Liu, and Z. Liu, "Synthesis and electrochemical performances of $(1–x)LiMnPO_4{\bullet}xLi_3V_2(PO_4)_3$/C composite cathode materials for lithium ion batteries," *Journal of Power Sources*, vol. 239, pp. 144–150, 2013.

[18] S. Liang, X. Cao, Y. Wang, Y. Hu, A. Pan, and G. Cao, "Uniform $8LiFePO_4{\cdot}Li_3V_2(PO_4)_3$/C nanoflakes for high-performance Li-ion batteries," *Nano Energy*, vol. 22, pp. 48–58, 2016.

[19] J. Zhang, C. Shen, B. Zhang et al., "Synthesis and performances of $2LiFePO_4{\bullet}Li_3V_2(PO_4)_3$/C cathode materials via spray drying method with double carbon sources," *Journal of Power Sources*, vol. 267, pp. 227–234, 2014.

[20] S. Zhong, L. Wu, J. Zheng, and J. Liu, "Preparation of high tap-density $9LiFePO_4{\bullet}Li_3V_2(PO_4)_3$/C composite cathode material by spray drying and post-calcining method," *Powder Technology*, vol. 219, pp. 45–48, 2012.

[21] C. Gao, H. Liu, G. Liu, J. Zhang, and W. Wang, "High-rate performance of $xLiFePO_4{\cdot}yLi_3V_2(PO_4)_3$/C composite cathode materials synthesized via polyol process," *Materials Science and Engineering B*, vol. 178, no. 4, pp. 272–276, 2013.

[22] Y. Si, Z. Su, Y. Wang, T. Ma, and J. Ding, "Improved electrochemical properties of $(1 - x)LiFePO_4{\cdot}xLi_3V_2(PO_4)_3$/C composites prepared by a novel sol-gel method," *New Journal of Chemistry*, vol. 39, no. 11, pp. 8971–8977, 2015.

[23] Y. Guo, Y. Huang, D. Jia et al., "Preparation and electrochemical properties of high-capacity $LiFePO_4–Li_3V_2(PO_4)_3$/C composite for lithium-ion batteries," *Journal of Power Sources*, vol. 246, pp. 912–917, 2014.

[24] S. Zhong, L. Wu, and J. Liu, "Sol-gel synthesis and electrochemical properties of $9LiFePO_4{\cdot}Li_3V_2(PO_4)_3$/C composite cathode material for lithium ion batteries," *Electrochimica Acta*, vol. 74, pp. 8–15, 2012.